Condensation Heat Transfer on Actuated Thermally Enhanced Hydrophobic Tubes

by

Thomas Nordstog

A Thesis Presented in Partial Fulfillment
of the Requirements for the Degree
Master of Science

Approved April 2022 by the
Graduate Supervisory Committee:

Konrad Rykaczewski, Chair
Robert Wang
Shankar Devasenathipathy

ARIZONA STATE UNIVERSITY

May 2022

ABSTRACT

Dehumidifiers are ubiquitous and essential household appliances in many parts of the world. They are used extensively in tropical and sub-tropical environments to lower humidity in living spaces, where high ambient humidity can lead to numerous negative health effects from mild physical discomfort to more serious conditions such as mold build up in structures and dangerous illnesses in humans. Most common dehumidifiers are based on conventional mechanical refrigeration cycles, where the effects of condensation heat transfer play a critical role in their effectiveness. In these devices, humid ambient air flows over a cold evaporator, which lowers the temperature of the humid ambient air below its dew point temperature and therefore decreases its water content by causing liquid water condensation on the evaporator surface. The rate at which humidity can be extracted from the ambient air is governed in part by how quickly the evaporator can shed the condensed droplets. Recent advances in soft, stretchable, thermally enhanced (through the addition of liquid metals) silicone tubing offer the potential to use these stretchable tubes in place of conventional copper pipe for applications such as dehumidification. Copper is a common material choice for dehumidifier evaporator tubing owing to its ubiquity and its high thermal conductivity, but it has several thermal downsides. Specifically, copper tubes remain static and typically rely on gravity alone to remove water droplets when they reach a sufficient mass. Additionally, copper's naturally hydrophilic surface promotes film-wise condensation, which is substantially less effective than dropwise condensation. In contrast to copper, thermally enhanced soft stretchable tubes have naturally hydrophobic surfaces that promote the more effective dropwise condensation mode

and a soft surface that offers higher nucleation density. However, soft surfaces also increase droplet pinning, which inhibits their departure. This work experimentally explores the effects of periodic axial stretching and retraction of soft tubing internally cooled with water on droplet condensation dynamics on its exterior surface. Results are discussed in terms of overall system thermal performance and real-time condensation imaging. An overall null result is discovered, and recommendations for future experiments are made.

ACKNOWLEDGMENTS

I would like to thank my advisor, Professor Konrad Rykaczewski, for the opportunity and mentorship, as well as my other committee members, Professor Robert Wang and Dr. Shankar Devasenathipathy for their assistance. Additional thanks to Dr. Praveen Kotagama, whose previous work in the fundamentals of soft stretchable thermally enhanced tubes laid much of the foundation for this study, and infinite thanks to my family for their love and support.

TABLE OF CONTENTS

LIST OF TABLES

LIST OF FIGURES

CHAPTER 1

INTRODUCTION AND BACKGROUND

1.1 Conventional Dehumidifiers: Benefits and Limitations

Dehumidifiers are common devices in both industrial and household settings, where their applications range from the drying of process air in chemical plants to the reduction of dampness in workplace buildings, which if left unabated has the potential to lead to a significantly increased chance of contracting mold related illnesses [1]. Dehumidifiers are typically based on conventional mechanical vapor-compression cycles utilizing an internally contained and pressurized refrigerant as a working fluid [2]. A generic thermodynamic cycle and functional diagram for a conventional vapor-compression refrigeration cycle used as a dehumidifier is shown in Figure 1.1.

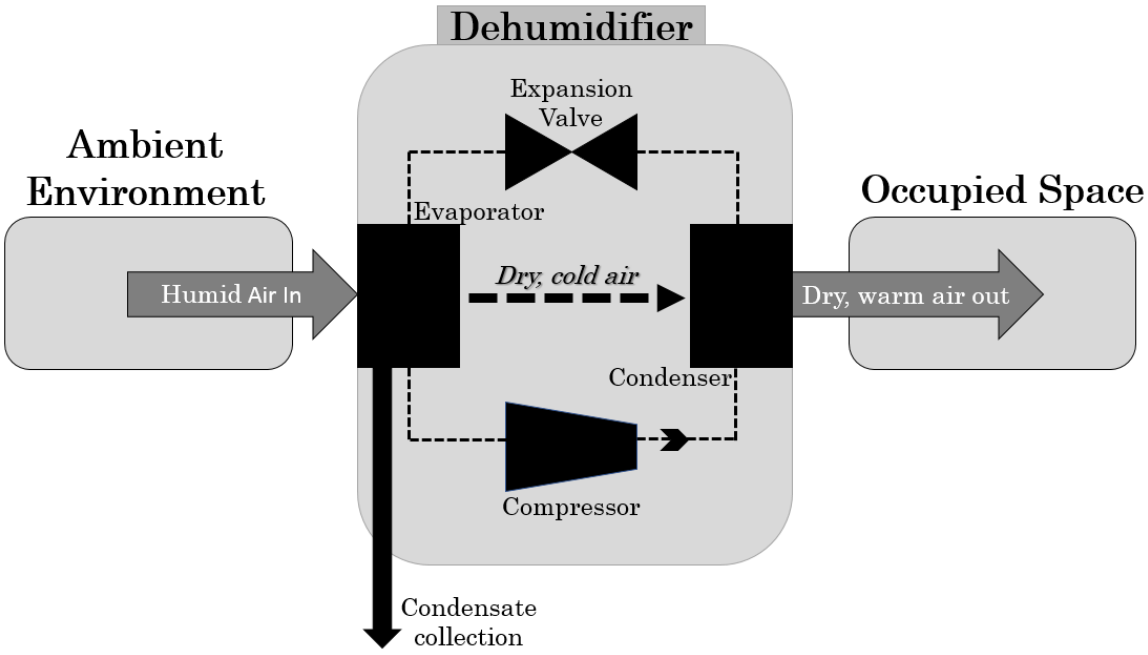

Figure 1.1: Conventional Dehumidifier

In these devices, the evaporator device is typically a coil of static copper tubes with attached fins to increase effective surface area for improved heat transfer and condensate collection. The expansion and subsequent evaporation of the internally contained and pressurized refrigerant causes the refrigerant to drop in temperature, causing the evaporator and its fins to likewise drop substantially below the ambient temperature. Separate from the self-contained refrigeration loop, an electric fan is used to draw in humid ambient air (the air to be dehumidified) from the environment and direct it over the cold evaporator. The temperature of the humid ambient air begins to drop due primarily to convective heat transfer between the air and the evaporator. Hot air is capable of holding substantially more water vapor than cold air; therefore, when the humid ambient air temperature drops, its capacity for holding water vapor drops as well, and the relative humidity (or RH) of the humid ambient air begins to rise [3]. The RH can be defined as the percentage ratio between P_v (partial vapor pressure of water vapor in humid air, Pa) and P_{sat} (saturation pressure of water vapor at a given environmental temperature and pressure, Pa) [3]:

$$RH = \frac{P_v}{P_{sat}} * 100\% \tag{1.1}$$

When $P_v = P_{sat}$, $RH = 100$ %, and the humid air can no longer retain all of its water vapor. Some of the water vapor therefore undergoes a phase change from vapor to liquid state, and condensate droplets form on the cold evaporator as a result. The threshold temperature at which this occurs for water undergoing a vapor to liquid phase transition is typically referred to as T_{dp} (dew point temperature, $°C$). After passing completely through the evaporator fins, the total water content of the

air has decreased due to the condensation on the evaporator, and therefore the absolute humidity of the ambient air has decreased as well. The absolute humidity is defined as the ratio of mass of water vapor per mass of dry air, and is often defined as [3]:

$$\phi = \frac{grams\ H_2O\ vapor}{kilograms\ dry\ air} \tag{1.2}$$

Although the ambient air is now cooled substantially below the ambient temperature and its absolute humidity is lower, its RH is relatively high. This is due to the previously mentioned effect of cold air being capable of holding substantially less water vapor than hot air. Air that is cold and has a high RH is typically not comfortable for humans, therefore the air is then directed over the warm condenser. The condenser surface is heated due to the compression (and subsequent condensation) of the internally contained and pressurized refrigerant. The temperature of the air rises due primarily to convective heat transfer between the cold air and the warm condenser, and the air's RH decreases as a result. The air then exits the condenser and into the conditioned environment as warm, dry air that is both safe and comfortable for occupants to breathe.

Of particular interest to this study is the choice of material for the evaporator tubing. Copper is typically used owing to its ubiquity, durability, ease of manufacture and assembly, and very high thermal conductivity ($k \sim 400\ Wm^{-1}K^{-1}$) [4]. The fins are typically either copper, aluminum ($k \sim 70 - 240\ Wm^{-1}K^{-1}$, depending on alloy) or steel ($k \sim 10 - 70\ Wm^{-1}K^{-1}$, depending on alloy) [4], most of which have fairly high thermal conductivities due to their metallic properties. The metal tubing and fins remain stationary during operation, and condensed droplets

quickly form a thin film that slowly accumulates and eventually drips off during operation.

This shedding of droplets through gravity alone can present some problems regarding condensation physics: if most of the evaporator surface is occupied by existing liquid film that has not yet been shed, this layer of liquid water on the evaporator can act as a layer of thermal insulation due to the relatively thick film ($L \sim mm$) and low thermal conductivity of liquid water ($k \sim 0.6\ Wm^{-1}K^{-1}$ [5]). If this thermal insulation effect is large enough, the heat transfer between the evaporator and the air may be reduced enough such that a substantially lesser amount of condensation occurs. The net effect is that the dehumidification performance can suffer if droplets are not frequently shed from the evaporator. Therefore, a dehumidifier that can utilize some mechanism other than gravity to periodically shed or remove these condensed droplets may offer significant improvements in dehumidification efficiency and performance. If a soft, flexible, and relatively thermally conductive tube material is used as the evaporator tubing, then stretching and relaxing of this tube is one potential physical mechanism that could be utilized to enhance droplet shedding and improve dehumidifier performance. One possibility for a device that fits these parameters is a soft thermally enhanced tube.

1.2 Soft Thermally Enhanced Tubes and their Applications

Heat exchanging thermal-fluidic industrial systems are made primarily of rigid metal components, due to the durability, ease of manufacture and assembly, and relatively high thermal conductivity of typical rigid metals. The rigidity of these heat exchanging thermal-fluidic systems stands in stark contrast to many of the

heat exchanging thermal-fluidic systems seen in biology, which typically have a much more flexible nature, permitting them to change their shape during operation. In these biological systems, dynamic shape-changing effects are an additional parameter that can be utilized to modulate heat transfer. For example, capillaries in the human body can automatically dilate or constrict to promote either heating or cooling to better regulate body temperature [6]. The addition of a novel shape-changing effect essentially adds an entirely new control knob to optimally govern thermal behavior in non-biological industrial systems and presents a potentially attractive option for creating industrial thermal-fluidic systems from soft shape-changing materials such as silicones. However, attempts to do so usually fall short of their desired thermal performance due to the low thermal conductivity of typical silicones ($k \sim 0.2\ Wm^{-1}K^{-1}$ [7]) in comparison to typical metals ($k \sim 10\ Wm^{-1}K^{-1}$ to $\sim 400\ Wm^{-1}K^{-1}$).

Recent advances in enhanced thermal conductivity liquid metal (LM) elastomer composites offer a potential solution to this challenge [8, 9, 10, 11]. In contrast to solid particles, room-temperature LM droplets can deform with the elastomer, enabling the retainment of many of the desired soft matter mechanical properties. These LM-elastomer composites have been shown to provide up to 600% extendibility even with up to 50% of the volume fraction being composed of LM [9]. They can increase the bulk thermal conductivity of the undeformed LM-elastomer composite to $\sim 3 - 7\ Wm^{-1}K^{-1}$ when the volume fraction of LM is 60-80%, and even show an intriguing extension-dependent anisotropic thermal conductivity effect, improving to $\sim 11\ Wm^{-1}K^{-1}$ anisotropic thermal conductivity when stretched when the volume fraction of LM is 60% [10]. Additional areas of active research on this

topic include improving the thermal conductivity of the LM itself [12, 13] and improving the bulk thermal conductivity of LM-elastomer composites through the introduction of small amounts of solid particles or other treatments [10, 14, 15, 16]. Given the breadth of active work on this topic, it is likely that the thermal conductivity of these soft thermally enhanced materials will continue to improve.

There are numerous potential industry applications for soft thermally enhanced materials, including personal heating / cooling in extreme environments [17, 18, 19] where the need for effective heat moving capability is well-proven [20, 21, 22], high powered robotics [23, 24, 25], soft biomedical robotics [26], temperature control of flexible heaters [27], improved personal garment cooling [28, 29], and improved fog harvesting, to name a few. Many of these potential applications would require the soft thermally enhanced material to be cast into a tube shape; for example, in garment cooling, the desired cooling effect could be obtained by flowing cold water through a series of soft flexible thermally enhanced tubes held in close contact with the body. Creating these tubes out of a thermally enhanced soft material would increase the tube's wall conductivity, decrease the net thermal resistance, and ultimately lead to improved body cooling compared to using a soft non-thermally enhanced material. In dehumidification/condensation applications, these soft thermally enhanced tubes could offer a number of advantages compared to regular soft non-thermally enhanced materials or potentially even conventional metals. To better explain these advantages, a brief discussion regarding the physics of condensation heat transfer on surfaces of different hardness is necessary.

1.3 Condensation Heat Transfer on Surfaces of Varying Hardness

When a substance below its critical temperature undergoes a phase transition from vapor to a liquid state, the substance temperature stays constant, but energy is released in the form of latent heat. The amount of latent heat energy released depends on the quantity of mass undergoing a phase transition as well as the substance's latent heat of vaporization (often interchangeably called "latent heat of evaporation" or "enthalpy of vaporization"), as defined below [3]:

$$Q = mL_v \tag{1.3}$$

Where Q is the amount of energy released (J), m is the total mass undergoing a phase transition (kg), and L_v is the latent heat of vaporization of the substance (J/kg). Assuming constant L_v, the time derivative of this equation can be taken to yield:

$$\dot{Q} = \dot{m}L_v \tag{1.4}$$

Where $\dot{Q}$ is the amount of energy released per second (W) and $\dot{m}$ is the quantity of mass that undergoes a phase transition per second (kg/s). For condensation, L_v arises primarily due to the internal energy released when molecular bonds are broken when transitioning from a higher internal energy vapor state to a lower internal energy liquid state, as well as due to a lesser effect corresponding to the mechanical work required for the change in the substance's volume. A fluid with particularly strong molecular bonding (such as the hydrogen bonds that dominate water's molecular structure) will have a correspondingly larger L_v, whereas a fluid with weaker bonds (such as a gas like helium which is held

together primarily by weaker van der Waals forces) will have a correspondingly lower L_v.

The latent heat of vaporization of a substance is a function of the environmental temperature and pressure at which the phase transition takes place, but for most engineering applications involving water near standard atmospheric pressure and temperature ($101325\ Pa, 293\ K$) it can be reasonably assumed to be a constant ($L_v \sim 2260\ kJ/kg$) [3]. The magnitude of L_v is identical for both a vapor-liquid transition as well as a liquid-vapor transition; the key distinction is whether the heat is added to the phase-transitioning substance (evaporation), or whether the heat is removed from the phase-transitioning substance (condensation). This effect is apparent in evaporative cooling [29], such as in human sweating, where the heat that must be added to the liquid sweat (primarily water) to undergo the liquid-vapor phase change must be removed from the body on which the liquid sweat resides.

The properties of the surface on which condensation is occurring will affect what is referred to as the condensation mode. Two general condensation modes exist: drop-wise condensation and film-wise condensation [30]. For drop-wise condensation, condensed liquid forms discrete droplets on the surface, whereas in film-wise condensation, condensed liquid forms a continuous liquid film on the surface. For heat transfer applications where it is typically desired to move the most amount of heat energy for a given temperature delta, dropwise condensation is strongly preferred due to its substantially higher heat-transfer-coefficient (HTC, $Wm^{-2}{}^{\circ}C^{-1}$), which can be at least ~ 5-7x higher versus film-wise [31]. This increase in HTC is due to the layer of thermal insulation that a continuous film of liquid

water creates in film-wise condensation and the possibility of more available nucleation sites with dropwise condensation vs film-wise condensation.

The selection of a particular condensation mode for a material is governed by the hydrophobic (or conversely, hydrophilic) properties of the material's surface. Liquid droplets on a hydrophobic surface will form visibly discrete droplets with a high contact angle, whereas liquid droplets on a hydrophilic surface will form a continuous liquid film with a low contact angle. A generic example of a low contact angle on a hydrophilic surface vs a high contact angle on a hydrophobic surface is shown below in Figure 1.2.

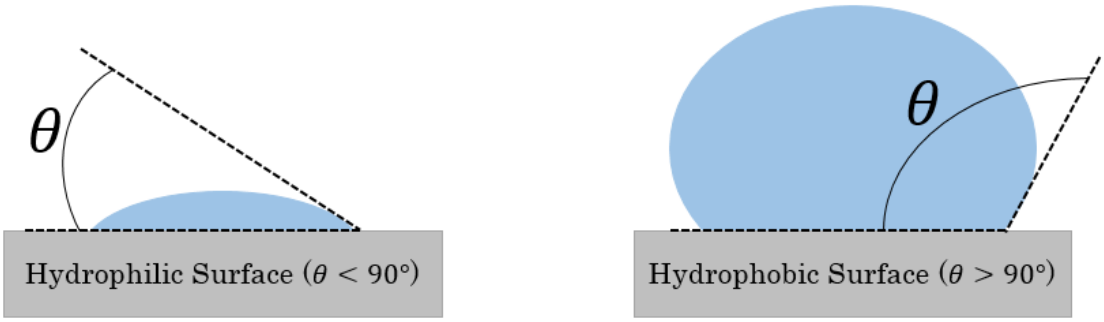

Figure 1.2: Hydrophilic and Hydrophobic Contact Angles

This hydrophilic vs hydrophobic distinction for a material is dictated by the material's surface energy (often interchangeably called "interfacial free energy" or "surface free energy"). Surface energy arises due to the fact that all solids must possess higher energy in the molecules at their surface compared to the molecules contained within the bulk of the material; otherwise, a continuous thermodynamic process of creating more surfaces through a solid-vapor phase transition (sublimation) would occur, and a solid state could not exist. This extra energy contained in the molecules at the surface of a material is referred to as surface

energy. The useful Young equation [32] shown below can be derived from a force balance on the interfaces of a liquid droplet on a flat rigid surface, and demonstrates a simple method for how surface energy can be estimated by contact angle measurements.

$$\gamma_{s-g} = \gamma_{s-l} + \gamma_{l-g}\cos(\theta) \tag{1.5}$$

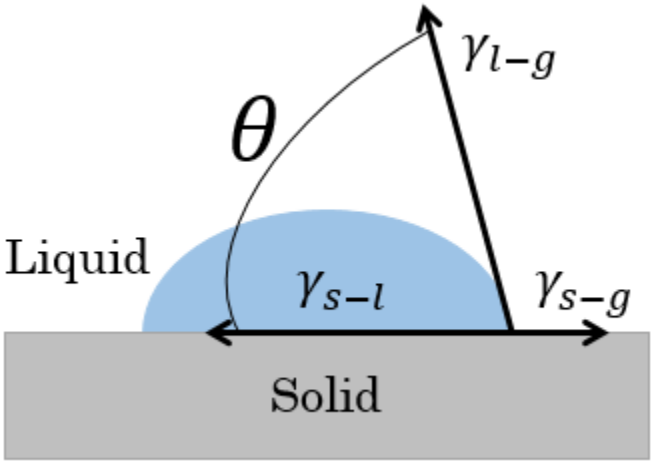

Figure 1.3: Force Balance on a Droplet

Where γ_{s-g} is the interfacial energy between the solid and gas phases (J/m^2), γ_{s-l} is the interfacial energy between the substrate and the liquid (J/m^2), γ_{l-g} is the interfacial energy between the liquid and gas phases (J/m^2), and θ is the contact angle (deg). Allowable values for θ range from 0° (perfect wetting) to 180° (non-wetting).

Soft materials also display another phenomenon referred to as droplet pinning. When a liquid droplet rests on a solid substrate, a small vertical wetting ridge is formed around the perimeter of the droplet. An example figure for a droplet on a soft substrate and its resulting wetting ridge shape are shown below, where the

wetting ridge is due to the combined effects of the Laplace pressure and the droplet's surface tension [33, 34, 35, 36, 37].

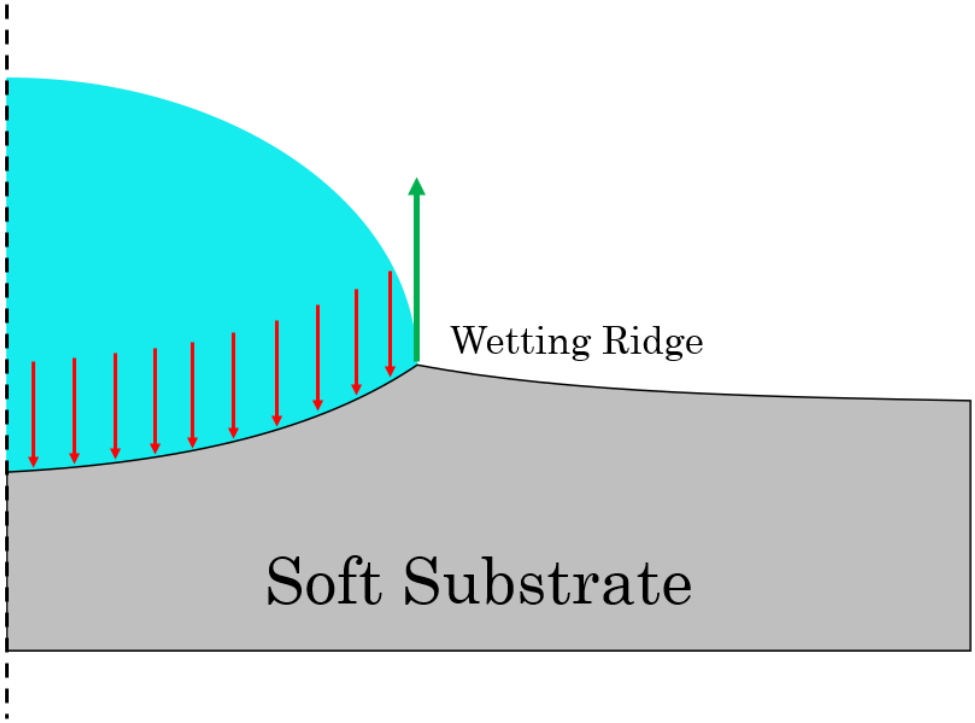

Figure 1.4: Droplet Pinning Effect

The height of this ridge affects the degree of droplet pinning; a ridge that is relatively high will more effectively pin the droplet to the substrate, while a ridge that is relatively low will have an overall negligible effect. The height of this ridge is heavily governed by the modulus of the substrate. For soft substrates with modulus ~75 kPa, the height of this ridge caused by a liquid water droplet is on the order of 1 μm, causing a notable droplet pinning effect; however, for hard substrates (such as metals) with modulus ~50 GPa, the height of this ridge is on the order of only 0.1 nm, causing a negligible droplet pinning effect [38]. Therefore, the droplet pinning effect is generally significant on most soft materials and generally negligible on most hard materials. If condensation heat transfer on a soft substrate is the desired

application, this droplet pinning phenomenon will act to hold the relatively low thermal conductivity liquid droplets to the surface, causing a net negative effect on overall heat transfer rates due to the introduction of additional thermal resistance through the low thermal conductivity liquid droplets.

Another phenomenon unique to condensation phase-transition on soft surfaces is the substantial increase in nucleation density modulated by the softness of the material. Sokuler et al. demonstrated [39] that reducing the modulus (i.e. increasing the softness) of a hydrophobic elastomer surface increases droplet nucleation density as well. They argue that this increase in droplet nucleation density is caused by the reduction in liquid-vapor interfacial area that is caused by a reduction in modulus, and that this therefore reduces the free energy barrier for nucleation. Additional research experimentally demonstrates an increase in condensation nucleation density on soft surfaces of $\sim 4x$ purely by reducing the modulus of a substrate from $500\ kPa$ to $100\ kPa$ [38].

The combined effect of these seemingly disparate phenomena is that soft materials, which generally have low surface energy and therefore intrinsically hydrophobic properties, will promote the much more effective dropwise condensation mode when compared to hard materials, as well as a higher nucleation density. At first glance and considering only the heat transfer occurring due to the vapor-liquid phase transition, these effects present a seemingly strong argument for using soft materials in lieu of hard materials in condensation heat transfer applications; after all, the heat transfer coefficient of dropwise condensation is typically at least ~ 5-7x that of film-wise condensation. This line of thought erroneously and detrimentally excludes the effect of heat conduction through the substrate, and the substantially

large differences in typical thermal conductivity between hard metals and soft materials (for example, there is ~3 ½ orders of magnitude difference in thermal conductivity between a typical soft silicone with $k \sim 0.2\, Wm^{-1}K^{-1}$ and copper with $k \sim 400\, Wm^{-1}K^{-1}$). This substrate heat conduction effect can have a significant effect on net heat transfer and overall condensation rates and must be quantified to understand the true advantage or disadvantage of soft materials in condensation applications.

To further illustrate this point, consider a generic example of sub-ambient temperature liquid water flowing in an annular tube, which is placed in a humid environment with ambient or above-ambient temperature and with convective heat transfer occurring on the exterior of the tube due to both sensible convective heating and condensation (where it is assumed that the temperature of the exterior of the tube is below the humid air's dewpoint temperature and therefore condensation is induced).

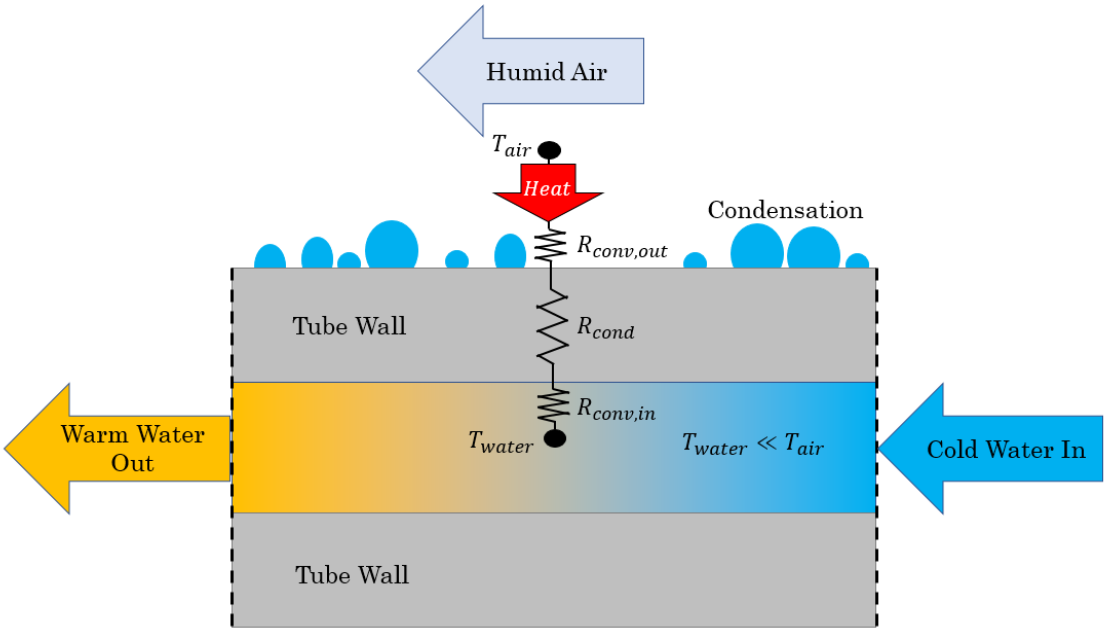

Figure 1.5: Simple 1D Annular Tube Heat Transfer Resistor Network

The total thermal resistance of this series 1D nodal network can then be written as:

$$R_{sys} = R_{conv,in} + R_{cond} + R_{conv,out} \tag{1.6}$$

Where R_{sys} is the total thermal resistance ($°C/W$), $R_{conv,in}$ is the internal convection resistance ($°C/W$), R_{cond} is the conduction resistance through the tube walls ($°C/W$), and $R_{conv,out}$ is the external convection resistance ($°C/W$). For maximum heat transfer with a given temperature delta, R_{sys} should be minimized. These individual resistance terms can be further expanded according to the standard forms of convective resistance and 1D conduction resistance through a tube wall [5] to yield:

$$R_{sys} = \frac{1}{h_{in}A_{in}} + \frac{\ln\left(\frac{r_{out}}{r_{in}}\right)}{2\pi k_{wall}L_{tube}} + \frac{1}{h_{out}A_{out}} \tag{1.7}$$

Where h_{in} is the internal convection resistance of the internal flow in the tube ($Wm^{-2}{}^{\circ}C^{-1}$), A_{in} is the internal area of the tube (m^2), r_{out} is the outer radius of the tube (m), r_{in} is the inner radius of the tube (m), k_{wall} is the thermal conductivity of the wall ($Wm^{-1}{}^{\circ}C^{-1}$), L_{tube} is the length of the tube (m), h_{out} is the outer convection resistance on the exterior surface of the tube ($Wm^{-2}{}^{\circ}C^{-1}$), and A_{out} is the outer area of the tube (m^2).

All other parameters and geometries being equal, a soft material that therefore promotes dropwise condensation and higher nucleation density on the exterior surface will increase h_{out} and reduce R_{sys}; however, soft materials generally have a much lower k_{wall}, which will increase R_{sys}. The relative increase or decrease of these two terms and their combined effect on R_{sys} determines whether the usage of a soft tube material in a hypothetical condensation application offers any improvements over a conventional hard metallic tube material.

1.4 Actuated Soft Thermally Enhanced Tubes as a Condenser

A choice of tube material that can simultaneously possess the aforementioned beneficial soft properties for condensation and additionally offer an increase in k_{wall} compared to typical soft materials may offer significant improvements over conventional metal materials in condensation applications. Furthermore, a tube that additionally enables mechanical movement may be able to use dynamic stretching and retracting to increase the frequency of adjacent droplet coalescence and shedding, increasing air dehumidification performance and improving condensation rates. One potential choice of tube material that fits these criteria is a soft thermally

enhanced tube that is periodically axially stretched and retracted by a separate actuation device, as shown in the figure below.

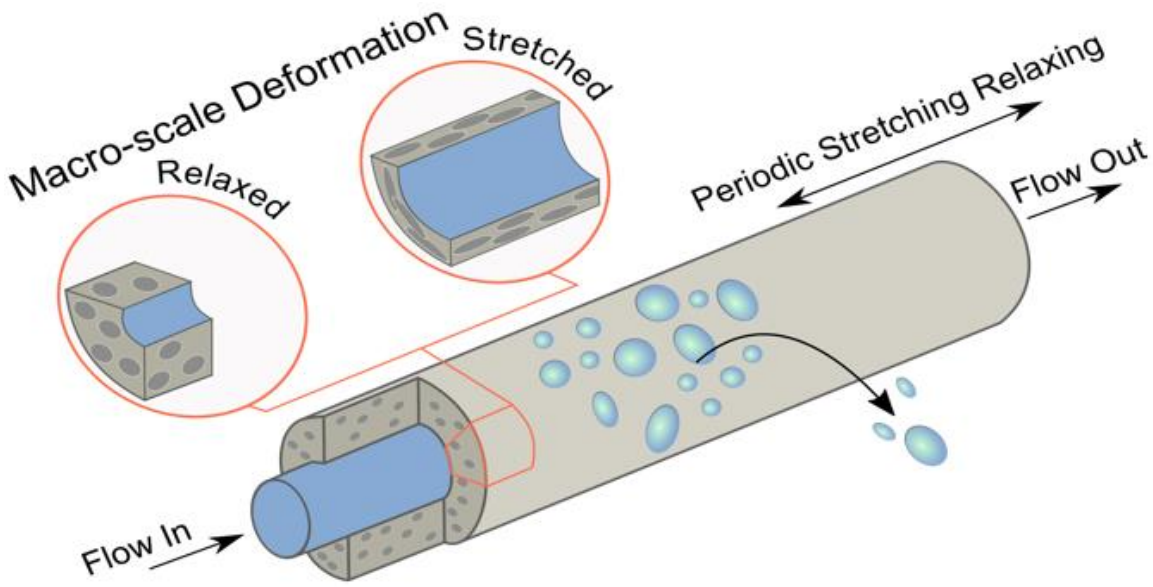

Figure 1.6: An Actuated Soft Thermally Enhanced Tube in Use

In this scenario, cold water flows through a thermally enhanced tube that is periodically stretched and relaxed. The ambient environment outside the tube is sufficiently hot and humid and the internal water flow is sufficiently cold so as to cause the exterior of the tube's surface to drop below the ambient air's dewpoint temperature, inducing condensation on the exterior of the tube and adding heat to the internal water through both a sensible heating (due to the temperature delta) and latent heating (due to condensation) effect. Because the device is both hydrophobic and soft, the condensation will occur as dropwise condensation with high contact angles and strong droplet pinning effects.

Although past work has explored the effect parameters such as nanoengineered materials [30], lubrication, and vibration [40] on improving

condensation, the available literature regarding the effect on condensation performance of stretching and relaxing of a soft thermally enhanced tube internally cooled by liquid water is (to the author's knowledge and at the time of writing) essentially non-existent. Thus, this work aims to address this gap. The subsequent chapters detail the fabrication, setup, tests, and results of a series of experiments designed to explore the effect of periodic axial stretching and relaxing of a soft thermally enhanced tube on condensation performance.

CHAPTER 2

EXPERIMENTS

2.1 Soft Thermally Enhanced Tube Fabrication

The soft thermally enhanced tubes are fabricated by combining a liquid 2-part silicone mixture with uncoalesced liquid metal (LM) droplets of a particular average droplet diameter and forming into an annular tube shape with a custom casting process. A 20% LM to 80% silicone (by volume fraction) mixture is used. This particular 20% LM mixture is chosen as a guard band based off past in-lab work where it is experimentally demonstrated that soft thermally enhanced tubes containing pressurized liquid water can break down and leak when the volume fraction of LM is greater than 30%. The particular liquid 2-part silicone mixture utilized is "Sortaclear 14" and the particular LM alloy is Galinstan.

Galinstan is a is registered trademark brand name referring to a eutectic alloy of gallium (Ga), indium (In), and tin (Sn). It is a non-toxic liquid metal with a melting point below room temperature, a relatively high thermal conductivity of $\sim 17\ Wm^{-1}{}^{\circ}C^{-1}$, and a relatively high electrical conductivity of $\sim 3.5 * 10^{6}\ Sm^{-1}$ [41]. Due to this unique blend of desirable properties (non-toxicity, flowable nature at room temperature, and high thermal/electrical conductivity), it has many present and potential industrial and research applications, including usage as a safe substitute for mercury in thermometers and telescopes [42], as flexible interconnects and electrodes for soft electronics [11, 43], and as a thermal interface material (TIM) for high power electronics cooling applications.

The exact mass fraction of Galinstan can vary slightly, but a targeted eutectic mass fraction split of ~68% Ga, ~22% Sn, and ~10% In is common. The Galinstan liquid metal filler particles as used in this work are made in-house. A final mass of 80 g of Galinstan is targeted to allow for at least one thermally enhanced tube with 20% volume fraction of liquid metal to be cast with sufficient Galinstan left over for additional casting (if needed) and miscellaneous characterization.

The pure gallium with a melting point slightly higher than room temperature is first melted by submerging the sealed bottle of gallium in a hot water bath. The desired mass of indium and tin are removed from bulk blocks of material with a manual chiseling and weighing process. Liquid gallium is pipetted out of the submerged bottle and the exact mass of gallium that is needed is dispensed into a glass container on a lab scale. The correct mass of indium and tin fragments are then added to the glass container. The solution is thoroughly mixed by hand and placed in a sealed oven at approximately $60°C$ overnight to allow each constituent element to fully diffuse and create the desired eutectic blend of Galinstan. This Galinstan can then be safely stored in its glass container at room temperature and used in a separate casting process to create a thermally enhanced tube.

First, Galinstan liquid metal droplets of the correct droplet diameter must be made. An appropriate amount of Galinstan for the final thermally enhanced tube (plus approximately 50% to spare) is dispensed into a glass test tube. A large amount of liquid ethanol is added so that the LM can be completely submerged. The mixture is subjected to high-speed shear mixing with a plastic stirrer chucked in a handheld Dremel rotary tool for approximately five minutes or until the average LM droplet diameter is $\sim 25 - 40\ \mu m$ as measured under an optical microscope. The

excess ethanol is then skimmed off the surface of the mixture with a syringe and discarded. An appropriate amount of 2-part silicone (by mass) is then added in a 1:1 (part A:B) mass ratio. The mixture is again subjected to high-speed shear mixing with a handheld Dremel rotary tool. Next, the mixture is placed in a vacuum chamber for approximately 10 minutes to remove all air pockets and evaporate any remaining ethanol. The result is a 20% LM silicone mixture that can then be cast into a thermally enhanced tube.

To fabricate the thermally enhanced tube, a glass tube (used here as a casting mold) that is 300 mm long with an ID of ~ 5.6 mm (McMaster Carr 8729K33) is vertically oriented with a test tube clamp. Note that the exact ID can vary slightly from glass tube to glass tube; since the glass tube is not reusable with this process, it should be noted that this can add dimensional variability from tube-to-tube. High-strength nylon fishing line (Catch All Tackle brand, SKU 2519933), suspended vertically by a shop vise, is run through the inner diameter of the glass tube to create what will be the hollow inner diameter of the thermally enhanced tube. The bottom of the glass tube is partially sealed with a custom-made rubber stopper. An automated syringe dispenser set to 0.5 ml/min is used to pump the 20% LM silicone mixture into the bottom of the glass tube. When the 20% LM silicone mixture is pumped to the top of the glass tube, the top is sealed with an additional custom-made rubber stopper. The nylon fishing line is then tensioned from the bottom with clamp-on weights so that its tensioned diameter is ~ 1.90 mm. The mixture is allowed to cure overnight at room temperature ($\sim 22°C$).

The thermally enhanced tube must then be extracted from the glass tube. The clamp-on weights are removed from the nylon fishing line and a glass tube

cutter is used to score and snap a small segment of the glass tube. Generous amounts of 99% isopropyl alcohol (IPA) are used as a lubricant when sliding off the cut-off piece of glass tube to reduce the chance of any silicone tearing. The process is then repeated down the length of the tube until all of the glass mold is removed. The thermally enhanced tube is then slid off the fishing line and any ragged ends are removed by making a square cross-cut with a razor. The fabrication process is then complete. The resulting thermally enhanced tube used in subsequent testing has an unstretched length of 271 mm, an unstretched ID of ~ 1.96 mm, and an unstretched OD of ~ 5.24 mm. Its mass is measured to be 11.2 g.

After fabrication, the same thermally enhanced tube is used for all subsequent thermal testing to remove any potential tube-to-tube variability that could arise due to minor inconsistencies in the casting process.

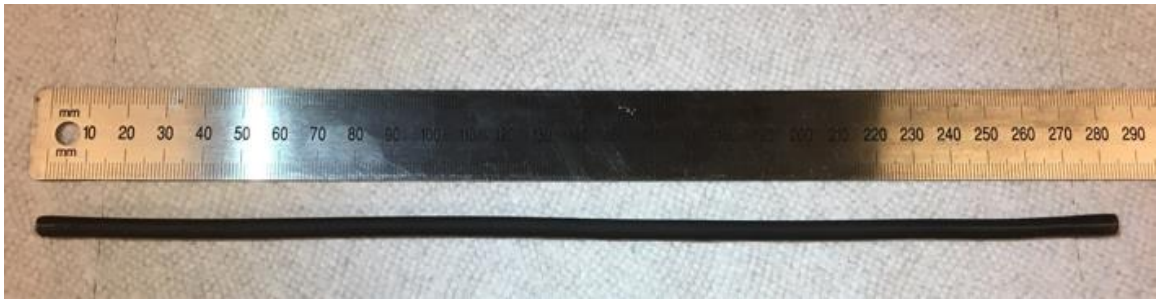

Figure 2.1: A Soft Thermally Enhanced Tube

2.2 Overall Experimental Setup

The primary question that this work aims to address is whether or not periodic axial stretching and retracting of a soft stretchable thermally enhanced tube can be used to improve droplet shedding in condensation applications. A

number of different experimental apparatuses are considered to investigate this phenomenon.

An optical criterion is considered, where growing and shedding droplets are continuously imaged throughout their lifecycle by a continuously running camera, and image analysis conducted in post processing is used to identify conditions where the droplet shedding is maximized. This concept is rejected due to the camera's limited field-of-view, issues with wall condensation blocking the camera's line of sight to the device-under-test (DUT, which in this context can refer either to a soft thermally enhanced tube or a copper tube), and difficulties with image processing algorithms over long timespans on both a moving and sagging object.

A mass transfer criterion is considered, where the mass of the shed droplets is directly measured by a scale placed underneath the DUT. The optimal droplet shedding conditions is indicated by the maximum mass of shed droplets captured over a given timespan. This method has been used successfully in past work [2], although the exact details of how the droplets are captured without affecting the system performance are unclear from the available information. This mass transfer criterion is rejected due to the difficulty in automated and real-time mass measurements from the available equipment, the difficulty in accounting for evaporation of shed droplets, and the difficulty in sealing the humid air environment around the DUT while simultaneously allowing for droplets to shed.

A heat transfer criterion is considered, where the optimal droplet shedding conditions is inferred by the overall system thermal resistance (lowest) and/or external heat transfer coefficient (highest). This criterion is selected due to the overall ease of thermal measurements compared to the aforementioned optical and

mass-transfer-based methods. The primary downside of this criterion is the overall low temperature deltas, which can lead to a relatively high experimental error, particularly when a minimal amount of heat is being added transferred; details are discussed further in Section 2.8.

A high-level functional block diagram of the overall heat transfer based experimental setup is detailed below.

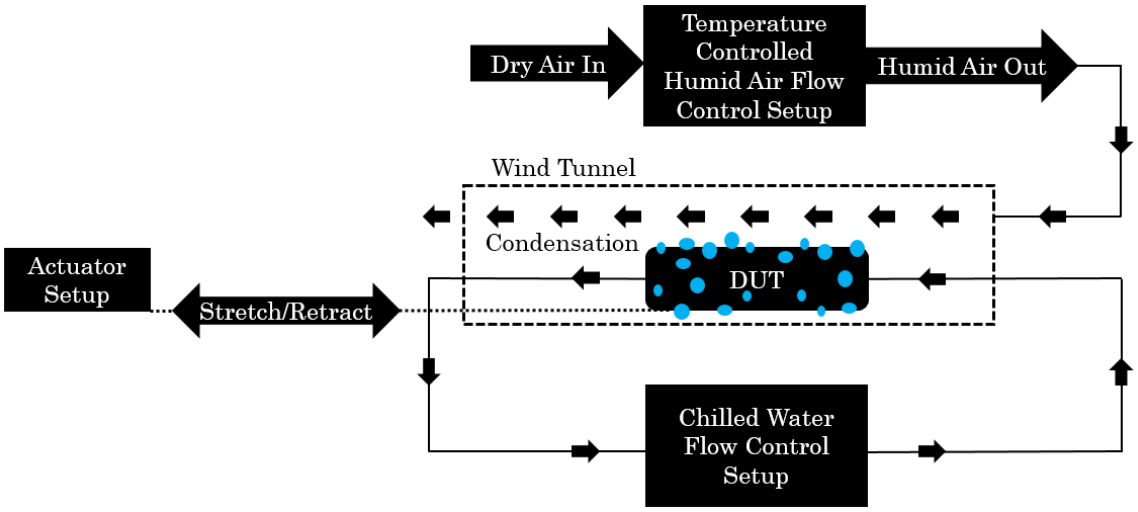

Figure 2.2: High-Level Experimental Functional Block Diagram

Chilled water is pumped through the DUT which is contained inside a sealed acrylic wind tunnel box constructed of 3/8" thick acrylic mechanically fastened with screws threaded into drilled and 6-32 tapped holes into the acrylic side panels. The tunnel is 45.5" long with an external width and height of 4" and 2 11/16" respectively. The edges of the wind tunnel are made as close to air-tight as possible with a combination of cut-to-length adhesive weather stripping and plumbing putty. The inlet side of the DUT is mechanically fastened to the tunnel such that the inlet side of the DUT cannot move during testing. Thermocouples measure the temperature delta of the chilled water across the DUT. A separate temperature

controlled humid air flow setup is used to flow either room temperature humid air or heated humid air through the tunnel and in a parallel flow arrangement (relative to the cooled water flow within the tube) across the DUT. As the room temperature or heated humid air flows across the cold DUT, the humid air's temperature drops rapidly until reaching its dewpoint temperature, which induces condensation on the exterior of the tube and adds energy to the water in the form of latent heat. A sensible heating effect also occurs due to the convective motion of the humid air across the DUT and the temperature delta between the air and the DUT. An electrically powered and programmatically controlled linear actuator is located just outside the outlet end of the wind tunnel. The actuator can be programmed to either remain stationary or continuously extend and retract its rod end at a user-controlled actuation rate. The actuator's rod end reaches into the tunnel where it is mechanically fastened to a sliding acrylic baseplate inside the tunnel. The outlet end of the DUT is also mechanically fastened to this sliding acrylic baseplate, such that as the linear actuator extends and retracts (such as when a thermally enhanced tube is actuated), the DUT extends and retracts too, creating the desired stretching and retracting motion in the tube. Multiple combined temperature and relative humidity (RH) sensors are used to read the temperature and RH of the humid air at three points in the tunnel, corresponding to the DUT inlet, the DUT outlet, and a point approximately midway across the DUT at its most extended length. Various DAQ (data acquisition) devices, the details of which are discussed in subsequent sections, are used to measure and record key test parameters to two separate test laptops (laptop #1 and laptop #2) running different DAQ scripts in parallel.

2.3 Cooled Water Flow Control Setup

A fluid loop consisting of an immersion chiller (VWR® model 89203-014), cooling coil, peristaltic pump (OMEGAFLEX® FPU5-MT), custom-made pulse dampener, vacuum membrane (PermSelect PDMSXA-2500), vacuum pump (model RS-1), analog pressure gauge (0-30 psi scale), thermocouple reader (Stanford Research Systems model PTC10), and turbine flowmeter with digital output (Omega model FLR1000) are used to cool and pump deionized water through the DUT while providing relevant fluid flow measurements. A detailed functional block diagram of this cooled water flow control setup is shown below.

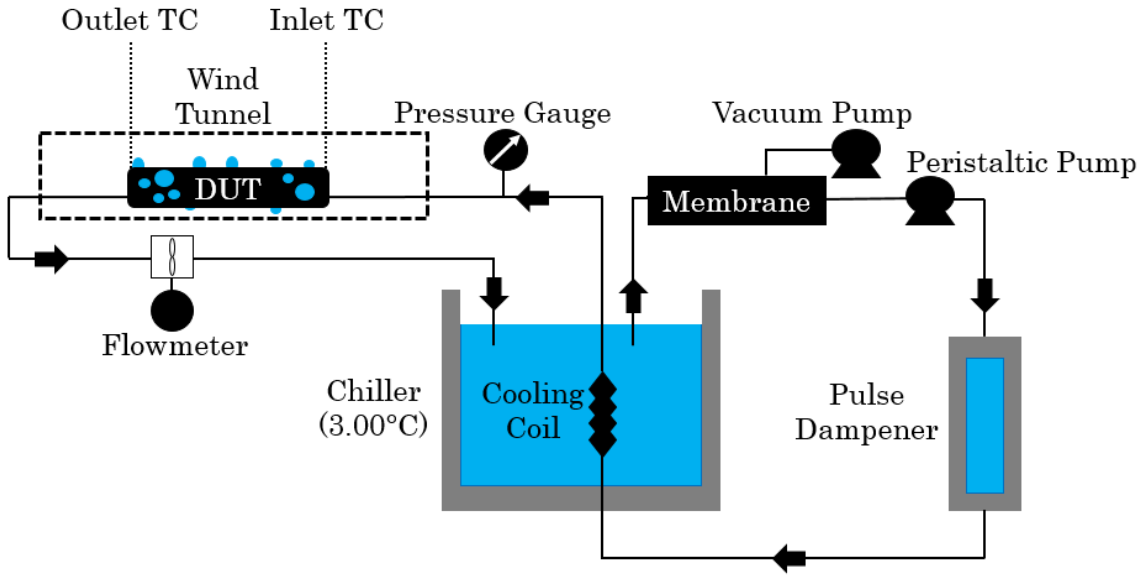

Figure 2.3: Water Flow Control Setup (Non-Critical Components Hidden)

The immersion chiller containing an unpressurized and unsealed reservoir of chilled deionized water is manually set to $3.00°C$, a setpoint which is maintained $\pm 0.1°C$ throughout the duration of the test. A peristaltic pump (manually set to a rate corresponding to $\sim 50\ ml/min$ measured output of water) connected upstream of

the chiller provides the suction needed to pump this ~ 3.0°C water from the immersion chiller and through a vacuum membrane connected to a continuously running vacuum pump, a process which removes the majority of any entrapped air within the water. The water then flows through the peristaltic pump and through a custom-made pulse dampener consisting of a vertically oriented PVC tube (2" diameter, ~21.5" tall) containing a static column of liquid water, which acts to dampen any unwanted sudden impulses in the water flow that can be introduced from the pulsing operating nature of a peristaltic pump. The water flow leaving the pulse dampener then moves through a sealed and coiled copper tube submerged within the immersion bath, which cools the water down. The water flow exits the coiled copper tube into an insulated section of tubing containing an analog pressure gauge, which is used as one metric to verify consistency of water flow from test to test, and then into the acrylic wind tunnel through a panel mount push-to-connect fitting that maintains the relatively airtight nature of the inlet side of the wind tunnel.

The plumbing sections within the wind tunnel and just before the DUT are insulated to reduce unwanted heat transfer from the environment to the cold water. In the center portion of the wind tunnel, a single DUT is attached between two plumbing sections using barbed fittings. The DUT can be either a thermally enhanced tube or a copper reference tube. The thermally enhanced tube can be attached directly to the barbed fittings, while the copper reference tube is attached via small pieces of flexible silicone tubing that are press fit on to the ends of the copper tube and then attached to the barbed fittings. Two 36-gauge T-Type SLE (Special Limit of Error) thermocouples are installed just before and after the DUT by

making small incisions in the plumbing tubing, inserting the thermocouples such that the welded thermocouple bead is centered in the flow, then sealing the incisions with ultraviolet (UV) cure epoxy and a UV light pen, which creates a water-tight seal. These thermocouples are located as close as feasible to the inlet and outlet side of the DUT, but the presence of adjacent fittings and a short run of plumbing tubing between the thermocouples and the DUT create an unavoidable additional path for heat to be added to the flowing liquid water that does not occur over the external area of the DUT. To mitigate this effect, these sections are wrapped with small amounts of aluminum foil to act as flexible and low-profile waterproof insulation. This effect is noted here as an appropriate caveat on the quantitative accuracy of the individual thermal resistance calculations in the latter half of Chapter 3.2.

As the water flows through the DUT, the external humid air flow adds heat to the water through both latent heat due to condensing droplets as well as sensible heat due to the convective motion of the humid air and the temperature delta between the humid air and the water. The thermocouples indicate the inlet / outlet temperature and resulting temperature drop of the water flow through the DUT and are measured by a thermocouple reader with a custom MATLAB script used to provide the serial interfacing and data logging functionality to laptop #1. The water exits the DUT and the outlet side of the wind tunnel and enters a turbine flowmeter where the flowrate is measured and translated to an analog output voltage read by an Arduino Uno running a custom Arduino IDE software script and recorded by laptop #1 using the freeware CoolTerm serial interfacing program developed by Roger Meier. The water is then dispensed back into the chilled water reservoir, where the process begins again and repeats in a continuous loop.

2.4 Temperature Controlled Humid Air Flow Control Setup

A temperature controlled humid air flow setup consisting of the laboratory's permanently plumbed adjustable compressed air supply, a digital volumetric gas flowmeter (Panasonic model FM-200), an analog pressure gauge (0-30 psi scale), a clear 4.5" OD PVC tube as a bubbler / hot water reservoir (McMaster #4740K52), a 6" long T-type threaded waterproof thermocouple probe (McMaster #1245N16) , a compact screw-plug 405W 120VAC immersion heater (McMaster #4668T56), and a benchtop temperature controller (Omega model CSi8DH-C24) are used to provide a steady flow of nearly saturated or saturated room-temperature or heated humid air to the wind tunnel. An ultrathin flexible probe T-type thermocouple (Omega Engineering), three HTU21D-F breakout board (Adafruit) temperature & humidity sensors, a TCA9548A I2C multiplexer breakout board (Adafruit), an Arduino Uno running a custom Arduino IDE software script, and laptop #2 with CoolTerm are used to measure and record air temperature and relative humidity at various key points within the wind tunnel itself. A process heater is attached in series with the flowmeter but is unused outside of preliminary testing. A detailed functional block diagram of this temperature controlled humid air flow control setup is shown below.

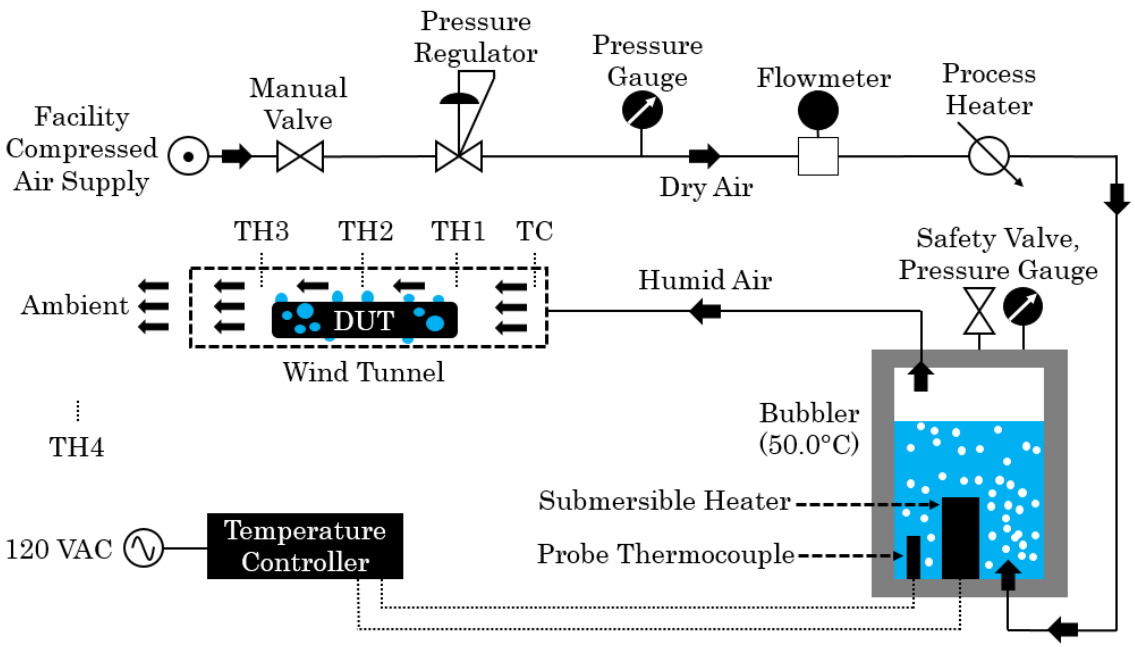

Figure 2.4: Humid Air Flow Control Setup (Non-Critical Components Hidden)

The bubbler / hot water reservoir (hereafter referred to only as the bubbler for brevity) is made from a 4.5" OD 48" long clear PVC pipe that is cut a final length of 33" long. PVC primer and cement are used to attach female-female PVC adapters to both ends, and large threaded PVC caps are attached with Teflon tape, pipe dope, and a strap wrench. These caps are manually drilled and then tapped to accept either 1/4 NPT or 1/2 NPT threaded fittings. The waterproof thermocouple probe, immersion heater, and an incoming dry air push-to-connect fitting are threaded to the bottom cap, while a pressure relief safety valve, analog pressure gauge, and outgoing humid air push-to-connect fitting are threaded to the top cap. The bubbler is kept in a vertical orientation and is filled partway with deionized water to approximately the 11/16 full mark at the beginning of every test. This height is chosen to maximize the volume of useable water while minimizing the amount of liquid water that may splash into the outlet port and subsequently enter the wind

tunnel. Incoming facilities air flows through an analog pressure gauge and a digital volumetric flowmeter, where the upstream dry air pressure and flowrate can be manually read and recorded, and then into the incoming dry air fitting mounted on the bottom cap of the bubbler and through the bubbler's water column.

As the air moves through the column of water within the bubbler, a rapid bubbling motion occurs, and the air's water vapor content increases rapidly. The air exits the top cap of the bubbler through the outgoing humid air fitting as saturated or nearly saturated humid air at approximately the same temperature as the bubbler setpoint. This humid air then flows through a short length of tubing and finally enters the wind tunnel, where it flows across the DUT in a parallel-flow configuration, and then exits the outlet side of the wind tunnel and ultimately into the ambient room environment. The incoming air's dry bulb temperature is measured within the wind tunnel immediately adjacent to the inlet by the ultrathin flexible probe T-type thermocouple mentioned previously and recorded by the PTC10 thermocouple reader to laptop #1. The three HTU21D-F temperature & humidity sensors mentioned previously are positioned within the tunnel (near the top left corner when facing the same direction as the air and water flow) at points corresponding to the inlet side of the DUT, the position approximately halfway across the stretched length of the DUT, and at the 45% extension mark of the DUT. These sensors are multiplexed and their temperature and humidity outputs are read by the TCA9548A I2C multiplexer and Arduino Uno and recorded to test laptop #2 with CoolTerm.

For the room temperature humid air test condition, the immersion heater in the base of the bubbler is left unpowered and the benchtop temperature controller is

left off. For the hot humid air test condition, the immersion heater is connected to the benchtop temperature controller, and the waterproof thermocouple probe in the base of the bubbler is used as the temperature reference. Due to the comparatively large thermal mass of the water column (~ $4L$ volume) and relatively low heater power ($\sim 405W$ @ $120VAC, 3.38A$), a simple automatic on-off control scheme is used with a setpoint of $50.0°C$ and a user specified dead-band of $0.5°C$. This controller configuration is found to maintain a suitably stable bubbler water temperature of $50.0°C$ ($+0.5°C$, $-1.0°C$). The bubbler and its outlet humid air lines are insulated to minimize heat losses to the environment that may contribute to undesired test variability.

2.5 Actuator Control Setup

An electrically powered and programmatically controlled linear actuator is used to provide the desired stretching and relaxing motion to the DUT over a range of 15-45% extension, corresponding to total DUT extended lengths of 312 mm to 393 mm, where the endpoints of the DUT is measured at the end of the DUT's stretched length on the barbed fitting. Note that this means the initial and end portion of the DUT (~10 mm on each side) are more thermally insulated (between the exterior humid air and the liquid water flowing within the DUT) due to the insulating effect of the DUT sliding over the plastic barbed fitting. Since the overall system thermal resistance is the primary criterion, and because this barbed fitting insulating effect is consistent from test-to-test, this is not detrimental; however, it should be noted, particularly as an appropriate caveat regarding the quantitative accuracy of the individual thermal resistance calculations later in Chapter 3.2. Two

different linear actuators are used depending on the desired actuation rate; a medium-speed actuator (Firgelli Automations FA-PO-240-12-8, max speed $\sim 13\ mm/s$) and a high-speed actuator (Firgelli Automations FA-PO-35-12-12, max speed $50\ mm/s$).

The actuator rod end extends into the outlet side of the wind tunnel, where it is mechanically fastened via a single screw to a sliding acrylic baseplate. This sliding acrylic baseplate is kept parallel to the interior of the wind tunnel with mechanically fastened aluminum L-channel guides contained within the wind tunnel. The outlet side of the DUT is mechanically fastened to this sliding acrylic baseplate, so that as the actuator moves, the DUT stretches and relaxes as well. A benchtop DC power supply (Yihua YH-305D) provides fixed 12VDC power to a DC motor controller (IBT-2 H-bridge). This motor controller outputs ±12 VDC PWM (pulse width modulated) power directly to the actuator power pins, where the PWM duty cycle corresponds to the desired actuator speed, and where the DC polarity corresponds to either extension (positive polarity) or retraction (negative polarity). The PWM duty cycle is user specified (0-100%) within a custom Arduino IDE software script. This script continuously reads the DUT's current extended position and provides either an extension or retraction signal to the motor controller depending on the desired limits of extension and the DUT's current extended position. The DUT's current extended position is read as a 0-5VDC signal by an Arduino Uno from the center pin of an embedded potentiometer within the actuator, where the +5VDC signal and ground reference are provided directly by the Arduino. An offline linear calibration is performed to match this 0-5VDC signal to the total extension length of the DUT with an actuator specific slope and intercept. Since the actuators are only rated for

20% on-time, a single 120-mm 12VDC computer case fan provides crossflow convective cooling to the actuator body and prevents overheating during continuous operation. Laptop #1 with CoolTerm is used to measure and record the DUT's current extended position throughout the entire duration of the test.

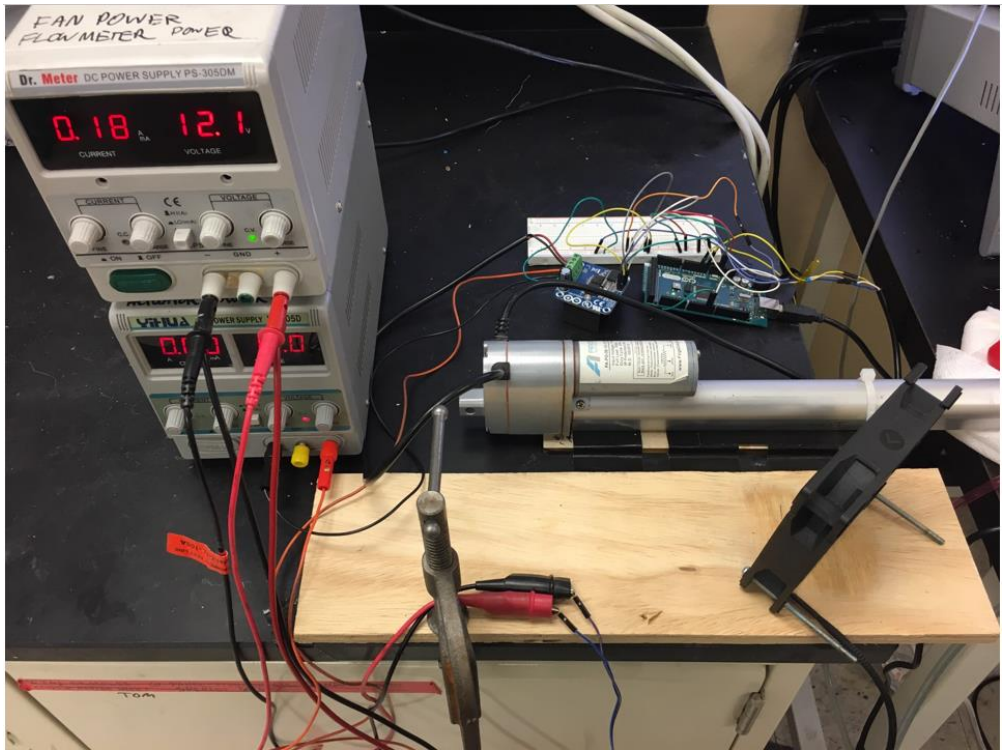

Figure 2.5: Actuator and Power Supply Setup

2.6 Design of Experiments and Procedure

A complete DOE (design of experiments) table is developed to investigate the effect of periodic axial and stretching of a thermally enhanced tube on droplet shedding and overall system thermal resistance. A variety of actuation rates, air temperature conditions, and DUT types are tested. A copper reference tube (McMaster Carr 8967K873), approximately as long as the thermally enhanced LM tube at 30% stretch and with as-close-as-possible to similar inner and outer

diameters, is used as a reference benchmark. The following table gives a high-level summary of tests performed and is ordered in a manner so as to emphasize readability; the actual tests are performed in a generally randomized order.

Table 2.1: Design of Experiments

Air State	**DUT**	**Actuation Rate (mm/s)**	**# Repeated Tests**	**Comments**
Room temp. humid air ($\sim 20°C\ dry\ bulb, 65-70\%\ RH$)	Thermally Enhanced LM Tube (15-45% stretch)	0 (hold at 30% stretch)	2	Benchmark
		1	2	
		5	2	
		9	2	
		25	2	
	Copper Tube	N/A	2	Benchmark
Hot humid air ($\sim 44-45°C, 100\%\ RH$)	Thermally Enhanced LM Tube (15-45% stretch)	0 (hold at 30% stretch)	3	Benchmark
		6	1	
		13	3	
		19	1	
		25	3	
	Copper Tube	N/A	3	Benchmark

A detailed and rigorously followed test procedure is developed. The following test procedure is used for both room temperature humid air and hot humid air tests,

with both the thermally enhanced LM tube and the static copper tube. Where applicable, differences between test conditions are noted.

1. The bubbler is topped off to the fill line ($\sim 4L$) with DI (deionized) water and the chiller is topped off (if necessary) with DI water.
2. The vacuum pump is checked for oil level and topped off if necessary.
3. The chiller is turned on and set to a $3.0°C$ setpoint. If hot humid air is desired, the bubbler temperature controller is turned on and set to a $50.0°C$ setpoint. If room temperature humid air is desired, the bubbler temperature controller is left off. The bubbler (if heated) and chiller each take ~ 30 minutes to reach their target setpoint, during which time the operator can continue to the next steps.
4. The desired actuator speed rate is set by manually modifying the PWM setting in the Arduino IDE script on laptop #1 and uploading to the actuator Arduino. If running either a static thermally enhanced LM tube or a copper tube condition, the actuator is first manually moved to its desired stationary length, and the actuator speed rate within the script is set to a zero PWM setting corresponding to $0\ mm/s$ (stationary).
5. The DUT is attached to the barbed fittings and its exterior is thoroughly cleaned with 99% IPA and dried with lint-free lab wipes.
6. The incoming dry air supply line is connected to the facilities supply. A low dry air volumetric flow rate of $\sim 5\ L/min$ is set by manually adjusting the facilities supply knob and manually reading the output of the digital flowmeter. This low flow rate ensures adequate mixing in the bubbler and low loss of water to the environment. The bubbler is left to vent to ambient.

7. The benchtop lab power supply that powers the actuator fan and flowmeter is turned on and manually set to 12VDC.
8. The 3x TH sensors are manually positioned at their respective locations within the wind tunnel.
9. The wind tunnel lid is attached with to the wind tunnel walls with screws. Any gaps in the sealing are patched with plumbing putty.
10. The external lighting (used for higher quality image taking) is turned on and positioned towards the DUT. If pictures / videos are being taken, the DSLR (digital single lens reflex) camera is positioned on its tripod facing the DUT center.
11. On laptop #1, a MATLAB initialization script is run one time to establish initial serial communications with the PTC10 thermocouple reader. The CoolTerm serial interfacing program is opened and set to begin running the actuator and recording actuator and flowmeter data when manually prompted.
12. On laptop #2, the CoolTerm serial interfacing program is opened and set to begin recording TH sensor data when manually prompted.
13. The operator pauses until the bubbler and chiller reach approximate thermal equilibrium. Once the bubbler and chiller are within $\pm 1°C$ of their target setpoint, the test is ready to begin. Proceed to the following steps.
14. The incoming dry air supply line is set to 50 L/min ($\pm$ 5 L/min) by manually adjusting the facilities supply knob.
15. The actuator is turned on by activating its benchtop power supply and setting to 12VDC.

16. On laptop #1, the MATLAB data recording script is run. The CoolTerm serial interfacing program is set to begin recording data.
17. On laptop #2, the CoolTerm serial interfacing program is set to begin recording data.
18. The peristaltic pump is turned on and set to a flow rate corresponding to $\sim 50\ mL/min$ output.
19. The vacuum pump is turned on, and the vacuum membrane is manually blocked with a silicone plug.
20. The bubbler's humid air output is connected to the wind tunnel input.
21. Manually note the time; this is the test start point. The target total test time is 3 ½ hours (210 minutes) for consistency from test-to-test.
22. Towards the end of the test, the water flowrate is manually measured by totalizing the flow output in a graduated beaker over one minute. The water flow pressure, as well as the incoming dry air volumetric flow rate & pressure, are manually recorded.
23. When 210 minutes have passed, the test can be ended. All data acquisition programs are manually shut off.
24. The incoming dry air supply, the benchtop power supplies, the peristaltic pump, the vacuum pump, the bubbler temperature controller, and the chiller are manually shut down.
25. The wind tunnel lid is removed, and the exterior of the DUT / copper tube is thoroughly dried with compressed air.

26. If using the stretchable LM DUT, the LM DUT is manually set to 15% extension (so as to not leave in an unnecessarily stretched state for a prolonged period of time).
27. The data files are manually transferred from laptop #1 and laptop #2 for post processing, as detailed in the subsequent section.

2.7 Data Post Processing and Experimental Parameters of Interest

Many test parameters are recorded for overall completeness, offline testing, and offline troubleshooting purposes, but only a subset of these parameters are used to any significant degree in subsequent post processing and to attain the results outlined in Chapter 3. The full test parameter table, which lists the test parameters collected, their data source, and any other relevant details, can be found in Appendix A located at the end of this document. A simplified test schematic displaying only the relevant quantities used in subsequent post processing and calculations is shown below.

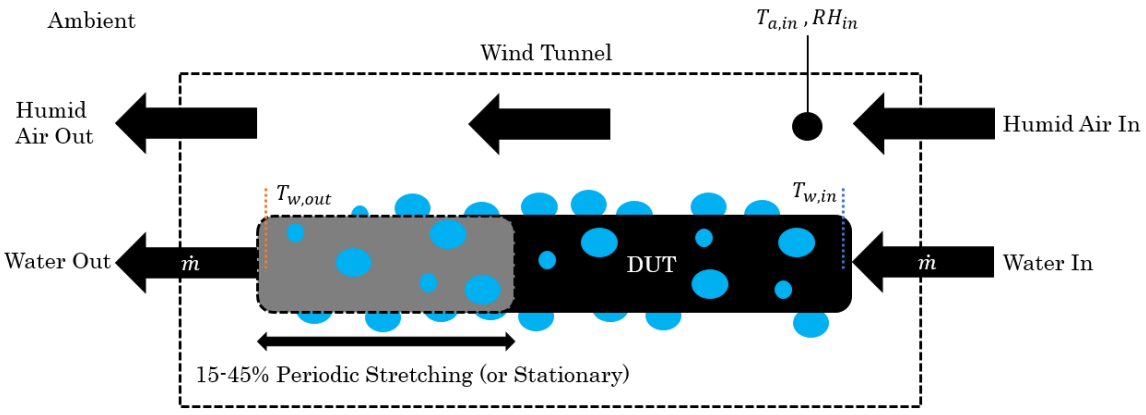

Figure 2.6 Relevant Quantities Used in Post Processing

As discussed in Section 2.2, a heat transfer criterion is selected for quantifying the effect of periodic stretching and relaxing on droplet shedding. Two figure-of-merits are considered: either a back-calculation of h_{out} as a function of different actuation rates, or a direct calculation of the overall system thermal resistance R_{sys} as a function of different actuation rates.

The h_{out} criterion requires precise knowledge of the DUT geometry and material thermal conductivity. The stretched inner and outer diameters of the DUT can be theoretically calculated by knowing the unstretched inner diameter, outer diameter, and the material's Poisson ratio with the following equation:

$$\frac{D}{D_o} = \left(\frac{L}{L_o}\right)^{-\nu} \tag{2.1}$$

Where D is the inner or outer diameter at a particular stretch (m), D_o is the unstretched inner or outer diameter (m), L is the length at a particular stretch (m), L_o is the unstretched length (m), and ν is the material's Poisson ratio $(unitless)$. For soft silicones, $\nu \sim 0.49$ [44]. Quantifying the unstretched dimensions of a soft thermally enhanced tube is non-trivial without destructive methods. The exterior diameter can be easily measured optically, but a precise measurement of the inner diameter requires the tube to be cross-sectioned at the points of interest and optically measured, destroying the tube in the process. Additionally, because the thermal conductivity of a soft thermally enhanced tube may change substantially as it is stretched [9, 45], a precise number for the effective thermal conductivity throughout the stretching cycle is difficult to attain. Therefore, the h_{out} criterion is

discarded in favor of a simplified and more robust approach that instead considers the overall system thermal resistance R_{sys}.

As can be seen in equation 2.1, R_{sys} is the sum of three series resistances: $R_{conv,in}$, R_{cond}, and $R_{conv,out}$. It is assumed that $R_{conv,in}$ and R_{cond} are consistent from test-to-test at a given actuation rate for the same DUT. Therefore, if actuation affects droplet shedding and therefore improves condensation, a reduction in $R_{conv,out}$ should be apparent by a corresponding reduction in R_{sys}. The overall system thermal resistance R_{sys} can be defined as a simple 1D resistance:

$$R_{sys} = \frac{\Delta T_{sys}}{\dot{Q}} \tag{2.2}$$

Where ΔT_{sys} is the system temperature delta ($°C$) and $\dot{Q}$ is the heat added to the water flowing within the DUT (W). The system temperature delta can be expanded in terms of the components in Figure 2.6 to yield an equivalent equation:

$$R_{sys} = \frac{T_{a,in} - T_{w,in}}{\dot{Q}} \tag{2.3}$$

Where $T_{a,in}$ is the incoming air dew point temperature ($°C$) (a common choice for condensation experiments and analysis [30]) and $T_{w,in}$ is the incoming water temperature ($°C$). Note that while a log-mean temperature delta is generally used in heat exchanger applications [5], a log-mean temperature delta typically implicitly assumes that the only energy exchange happening is occurring only between the two fluids of interest. This is not the case in this setup, since not all of the energy exchanged by the room temperature / hot humid air flowing over the DUT is deposited directly into the liquid water flowing through the DUT; some energy

exchange also occurs through the walls of the wind tunnel with the ambient environment. An additional downstream air temperature sensor, required for a log-mean temperature delta, also introduces additional experimental uncertainty, and it is dubious if it could adequately capture an accurate average air temperature across the complete air velocity profile due to its small sensor size. Additionally, the downstream TH3 sensor described earlier remains stationary at the 45% extension mark, and does not move with the DUT when stretching and relaxing is utilized. Therefore, it would not accurately capture the temperature drop of the flowing humid air as it occurs only over the DUT. Due to these effects, and since the qualitative behavior of R_{sys} as a function of actuation rate is the primary metric, the simpler $\Delta T_{sys} = T_{a,in} - T_{w,in}$ metric is utilized instead of a log-mean temperature delta.

The $\dot{Q}$ term in Equation 2.3 can be expanded with an energy balance of the DUT, yielding:

$$\dot{Q} = \dot{m} c_p (T_{w,out} - T_{w,in}) \tag{2.4}$$

Where $\dot{m}$ is the mass flowrate of liquid water through the DUT (kg/s), c_p is the liquid water's specific heat at constant pressure ($Jkg^{-1}K^{-1}$) which is assumed to be a constant value of 4169 $Jkg^{-1}K^{-1}$ (a reasonable value within ~0.2% of most common literature values [5]) and $T_{w,out}$ is the outlet water temperature ($°C$). Plugging this into equation 2.3 gives the following final expression for R_{sys} in terms of the relevant quantities shown in Figure 2.6:

$$R_{sys} = \frac{T_{a,in} - T_{w,in}}{\dot{m} c_p (T_{w,out} - T_{w,in})} \tag{2.5}$$

When hot humid air is used, the incoming air can be reasonably assumed to be completely saturated, and the incoming air dew point temperature $T_{a,in}$ is therefore just the dry bulb temperature as reported directly by the TH1 sensor. When room temperature air is used, the incoming air cannot be assumed to be completely saturated, as TH1 measurements show that its relative humidity is only $\sim 65-70\%$. Therefore, an equation is needed to calculate the incoming air's dew point temperature as a function of its dry bulb temperature and its relative humidity. The Magnus formula [46], itself derived from the Clapeyron-Clausius equation, is used:

$$T_{DP}(T,RH) = \frac{\lambda * \left(\ln\left(\frac{RH}{100}\right) + \frac{\beta T}{\lambda + T}\right)}{\beta - \left(\ln\left(\frac{RH}{100}\right) + \frac{\beta T}{\lambda + T}\right)} \tag{2.6}$$

Where constants λ and β are defined as $\lambda = 243.12°C$ and $\beta = 17.62$. Plugging in the dry bulb temperature T and relative humidity RH as measured by the TH1 sensor into this equation yields the corresponding dew point temperature T_{DP}, which is used as $T_{a,in}$ when calculating R_{sys} when room temperature humid air is used.

Studying the effect of actuation rates on R_{sys} makes the parameters of interest inherently transient and periodic. Therefore, time averaged values for the relevant parameters of interest over the final 10 minutes of testing are used. In order to guarantee a relatively steady state system (or at least to remove as much time constant dependence as possible), a total test time of exactly 210 minutes is targeted, where relevant parameters of interest are averaged over the final 200-210 minutes. At the lowest actuation rate of $\sim 1\ mm/s$, and considering that the soft thermally enhanced tube DUT being stretched over a $15-45\%$ stretch corresponds

to beginning and ending lengths of $312mm$ and $393mm$ respectively, the longest period that arises in the data will be approximately $162\ s$. Thus, time-averaging over 10 minutes guarantees at least three periods worth of data at the slowest actuation rate, which is a sufficient amount to remove any period dependent trends. These time-averaged values are then used in the equations shown above to calculate R_{sys} as a function of different actuation rates.

2.8 Experimental Uncertainty Analysis

A detailed error analysis is critical for any meaningful conclusions to be drawn from experimental data. One common method for approximating error in experimental measurements is to the split the total error ϵ_{total} into a bias error component ϵ_{bias} and a random error component ϵ_{random}. The total error can then be calculated due to the combined effects of these (assumed orthogonal and therefore independent) bias and random components:

$$\epsilon_{total} = \sqrt{\epsilon_{bias}^2 + \epsilon_{random}^2} \tag{2.7}$$

The bias error component ϵ_{bias} corresponds to errors due to uncertainty in parameters such as physical properties and test measurements, while the random error component ϵ_{random} corresponds to test-to-test uncertainty due to random and uncontrollable test inconsistencies and environmental factors. The bias error ϵ_{bias} can be estimated analytically while the random error ϵ_{random} is typically measured by examining the repeatability of the data with the same test conditions and procedure repeated multiple times in succession.

The Taylor Series approach [47] for estimating bias error ϵ_{bias} with a linear uncertainty propagation is utilized. Consider a generic function f, that itself is a function of n variables:

$$f = f(x_1, x_2, \dots x_n) \tag{2.8}$$

The bias error of f depends on the individual bias uncertainties corresponding to all n variables ($\epsilon_{x_1}, \epsilon_{x_2}, \dots \epsilon_{x_n}$). Assuming that the individual bias uncertainties are relatively small and that both the variables and their bias uncertainties are independent of each other, ϵ_{bias} can be estimated with a Taylor series expansion and subsequent truncation as:

$$\epsilon_{bias} = \sqrt{\left(\frac{\partial f}{\partial x_1}\right)^2 {\epsilon_{x_1}}^2 + \left(\frac{\partial f}{\partial x_2}\right)^2 {\epsilon_{x_2}}^2 + \cdots \left(\frac{\partial f}{\partial x_n}\right)^2 {\epsilon_{x_n}}^2} \tag{2.9}$$

The units of ϵ_{bias} are therefore identical to the units of f. As discussed previously in section 3.1.1, the main experimental parameter of interest is R_{sys} $(°C/W)$. Recall equation 2.5 from Section 2.7:

$$R_{sys} = \frac{T_{a,in} - T_{w,in}}{\dot{m} c_p (T_{w,out} - T_{w,in})} \tag{2.5}$$

The experimental bias uncertainty in the system thermal resistance R_{sys} can be calculated by applying equation 2.9 to equation 2.5, using the five independent parameters ($T_{a,in}, T_{w,in}, \dot{m}, c_p$, and T_w, out) directly from equation 2.5 as x_1, x_2, x_3, x_4 and x_5.

Five partial derivatives are required. These are calculated here as:

$$\frac{\partial R_{sys}}{\partial T_{a,in}} = \left(\dot{m}c_p\left(T_{w,out} - T_{w,in}\right)\right)^{-1} \tag{2.10}$$

$$\frac{\partial R_{sys}}{\partial T_{w,in}} = -\left(\dot{m}c_p\left(T_{w,out} - T_{w,in}\right)\right)^{-1} + \frac{T_{a,in} - T_{w,in}}{\dot{m}c_p\left(T_{w,out} - T_{w,in}\right)^2} \tag{2.11}$$

$$\frac{\partial R_{sys}}{\partial \dot{m}} = \frac{-T_{a,in} + T_{w,in}}{\dot{m}^2 c_p (T_{w,out} - T_{w,in})} \tag{2.12}$$

$$\frac{\partial R_{sys}}{\partial c_p} = \frac{-T_{a,in} + T_{w,in}}{\dot{m}{c_p}^2 (T_{w,out} - T_{w,in})} \tag{2.13}$$

$$\frac{\partial R_{sys}}{\partial T_{w,out}} = \frac{-T_{a,in} + T_{w,in}}{\dot{m}c_p\left(T_{w,out} - T_{w,in}\right)^2} \tag{2.14}$$

Reasonable estimates for the five individual bias uncertainty terms are assumed to be $\epsilon_{T_{a,in}} = 0.5°C$, $\epsilon_{T_{w,in}} = 0.1°C$, $\epsilon_{\dot{m}} = 1\ \frac{ml}{min} = 0.0000167\frac{kg}{s}$, $\epsilon_{c_p} = 8\ \frac{J}{kgK}$, and $\epsilon_{T_{w,out}} = 0.1°C$.

Plugging the 10 terms above into equation 2.10 will yield the estimated bias uncertainty in R_{sys} for a given test. As discussed in Section 2.7, time averaged values over the final 10 minutes are used for $T_{a,in}$, $T_{w,in}$, and $T_{w,out}$. A constant liquid water specific heat value is used, and water mass flow rate $\dot{m}$ is measured directly by manually totalizing and reading the volume of flow from a graduated test beaker over a span of 60 seconds near the end of the test. The final ϵ_{bias} for a given actuation rate is calculated as the average of all individual ϵ_{bias} (for each individual test) at that actuation rate.

As mentioned previously, the random error ϵ_{random} is typically estimated by examining the repeatability of the data with the same test conditions and procedure

repeated multiple times in succession. The specific method used here to estimate ϵ_{random} is to first calculate the standard deviations σ of the final parameter of interest R_{sys} at each nominal actuation rate. For example, if i different actuation rates are considered (rate 1, rate 2, … rate i), each with j different individual measurements of R_{sys} $(R_{sys,1}, R_{sys,2}, \ldots R_{sys,j})$ then i different standard deviations σ of R_{sys} can be calculated at each rate $(\sigma_1, \sigma_2, \ldots \sigma_i)$, where the "$i$th" standard deviation σ_i corresponding to the "ith" actuation rate is calculated according to the typical sample standard deviation formula:

$$\sigma_i = \sqrt{\frac{\sum_j \left(R_{sys,j} - \overline{R_{sys}}\right)^2}{j-1}} \tag{2.15}$$

Where the overbar operator in this context refers to the arithmetic mean. A single average standard deviation σ_{avg} corresponding to the average of all standard deviations over all "i" actuation rates can then be calculated with:

$$\sigma_{avg} = \frac{\sum_i \sigma_i}{i} \tag{2.16}$$

The random error ϵ_{random} can then be calculated at any sigma-limit (often given at 1, 2, or 3-sigma limits, corresponding to ~68%, ~95%, and ~99.7% confidence intervals respectively) with:

$$\epsilon_{random} = \beta \sigma_{avg} \tag{2.17}$$

Where β is the desired sigma-limit. All subsequent calculations assume a 2-sigma ($\beta = 2$), corresponding to a ~95% confidence interval.

The total error ϵ_{total} for a given data point is displayed in all subsequent sections as vertical +/- error bars centered on the data point. If only one data point is available for a given actuation rate, ϵ_{random} is assumed to be the average of the ϵ_{random} values at the two closest actuations rates. Error in actuation rate is assumed to be negligible.

CHAPTER 3

RESULTS

3.1 Room Temperature Humid Air Results

Room temperature humid air ($\sim 20°C\ dry\ bulb, 65-70\%\ RH$) with light convective parallel flow tests are conducted according to the parameters specified in Table 2.1. Multiple tests are conducted on a soft thermally enhanced tube at various actuation rates as well as on a static copper reference tube as a benchmark. The raw system thermal resistance R_{sys} is plotted as a function of the tube's nominal actuation rate (mm/s) and displayed as individual data points below.

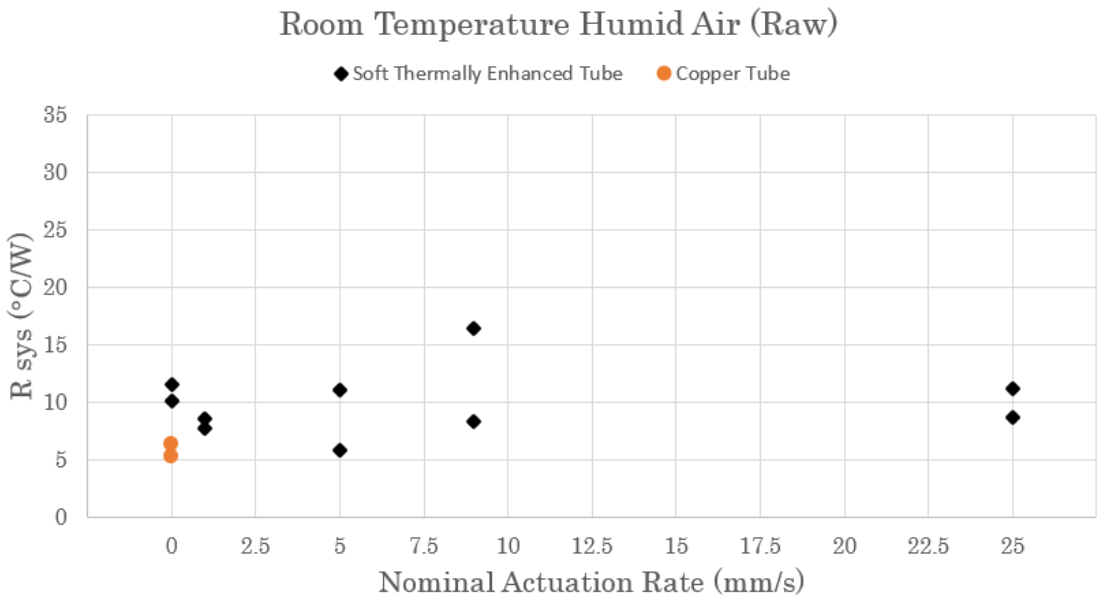

Figure 3.1: Room Temperature Humid Air Raw Data

A non-dependent relation between R_{sys} and the nominal actuation rate is seen from the raw data. It is observed that adjusting the nominal actuation rate does not appreciably change the R_{sys} values for the soft thermally enhanced tube.

Therefore, under these room temperature humid air conditions, adding periodic mechanical stretching and retracting to a soft thermally enhanced tube does not appear to cause a detectable change in net condensation heat transfer. It is also observed that the copper reference tube, as might be expected a priori, is generally the lowest R_{sys}. These results are confounded by the overall low temperature drop ($\sim 0.2°C - 0.4°C$) occurring across the water flowing through the DUT, which adds a significant amount of bias uncertainty. Accounting for the total uncertainty, the averaged R_{sys} values at each actuation rate, along with corresponding error bars encompassing bias and random uncertainties, are displayed below.

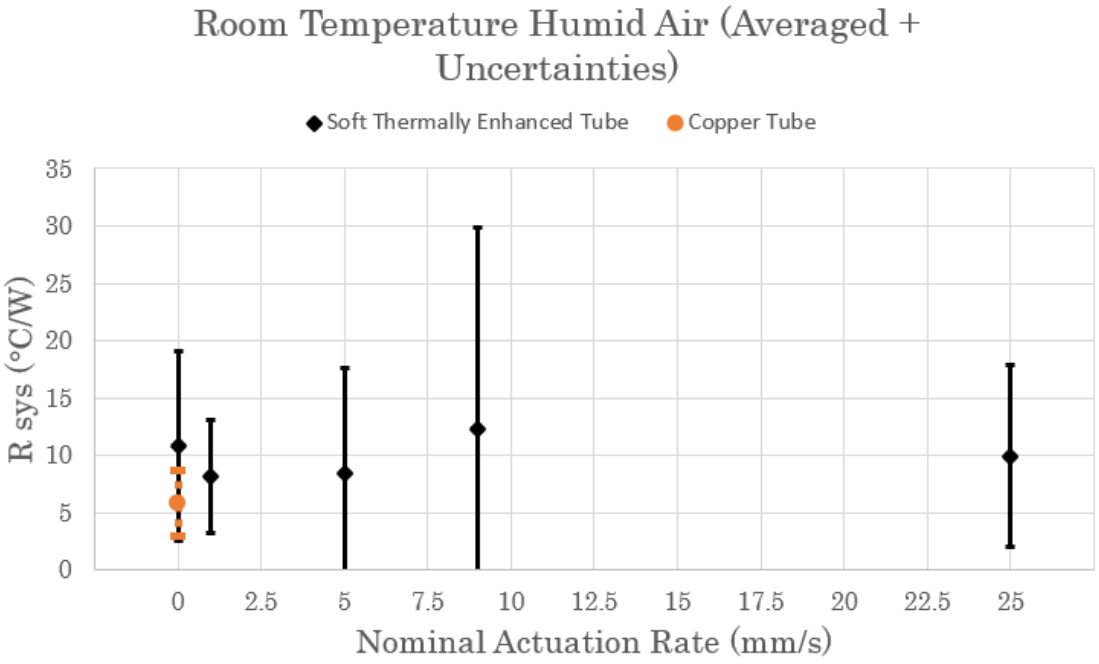

Figure 3.2: Room Temperature Humid Air, Averaged Data with Uncertainties

Again, a non-dependent relation between R_{sys} and the nominal actuation rate is observed. High uncertainty bias uncertainty in the temperature drop measurements adds significant overall uncertainty and large error bars. The overall

error bars for the soft thermally enhanced tube at each actuation rate overlap with each other, as well as with the static copper tube, indicating that no statistically significant effect of nominal actuation rate on R_{sys} can be observed with this test apparatus, these devices, and under these test conditions.

Due to these large error bars under room temperature humid air conditions, the focus of testing will instead shift to hot humid air conditions, where a higher temperature drop across the water flowing through the DUT significantly shrinks the bias uncertainty. The results of these hot humid air tests are displayed further in Section 3.2.

Although no statistically valid dependence on R_{sys} can be observed, the usage of room temperature humid air means that the walls of the wind tunnel are above the local dew-point temperature, leading to no visible wind tunnel wall condensation and allowing an unobstructed line-of-sight to the DUT for an external camera to capture live-images of the condensation nucleation, growth, and departure, allowing for an insightful qualitative look into the condensation dynamics and timescales.

Side-view images are shown below for room temperature humid air dropwise condensation on a static thermally enhanced tube over the initial droplet growth stage as well as throughout the later stages of the same test. The same timescales are shown for film wise condensation on a static copper tube. Finally, images are shown for a stretching and retracting (nominal actuation rate 9 mm/s) thermally enhanced tube throughout one complete actuation cycle.

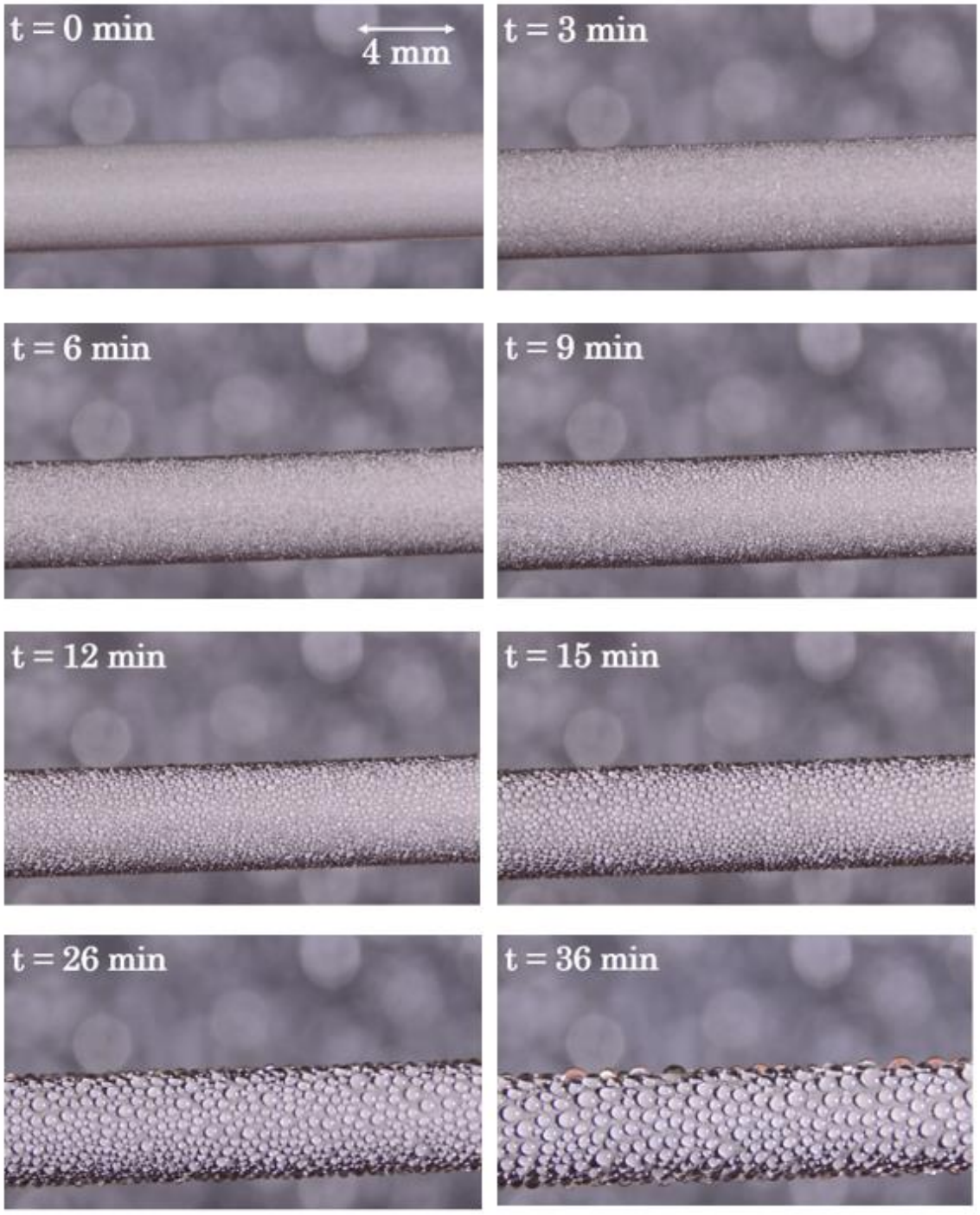

Figure 3.3: Room Temperature Humid Air, LM, Initial Dropwise Condensation, Static

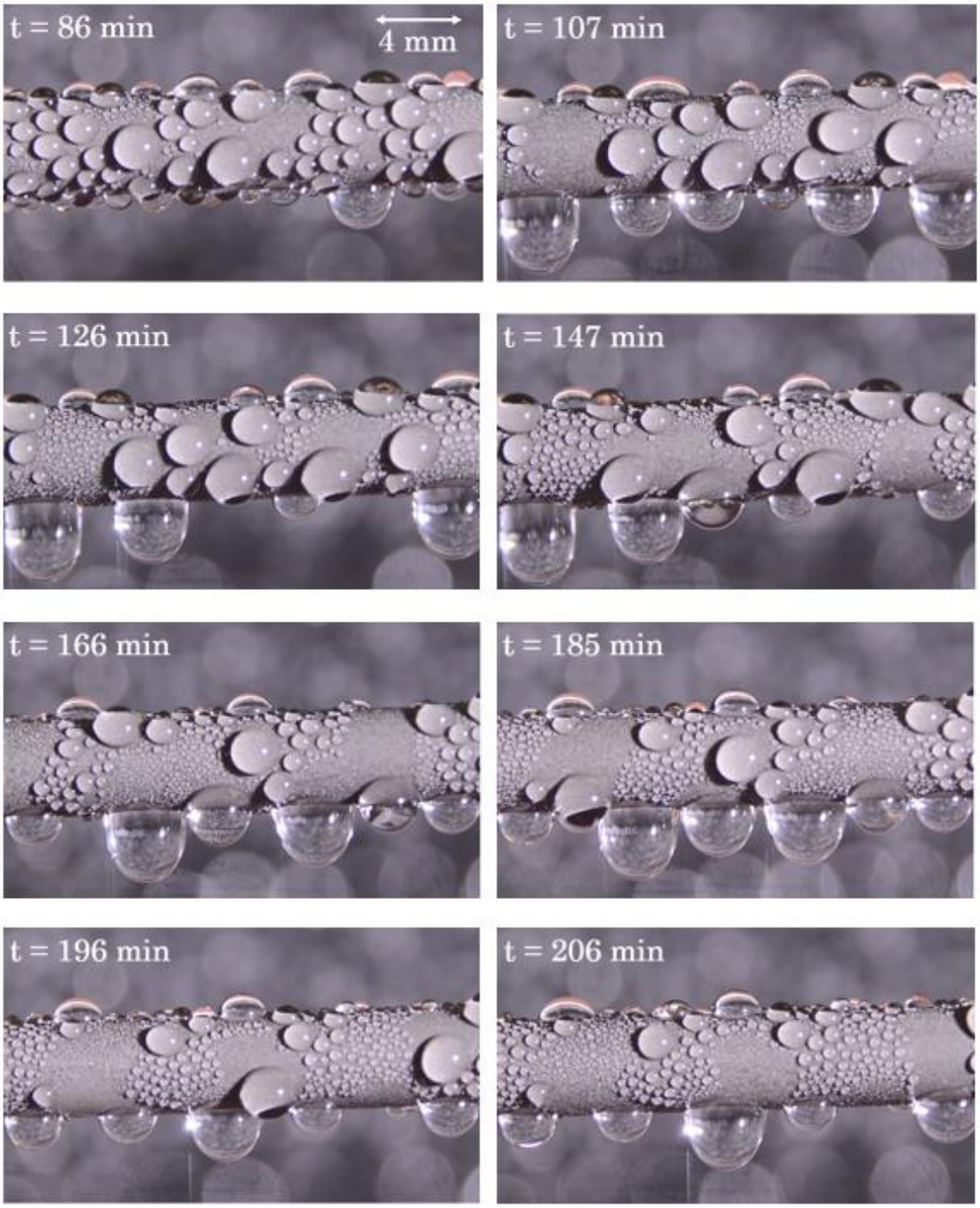

Figure 3.4: Room Temperature Humid Air, LM, Later Dropwise Condensation, Static

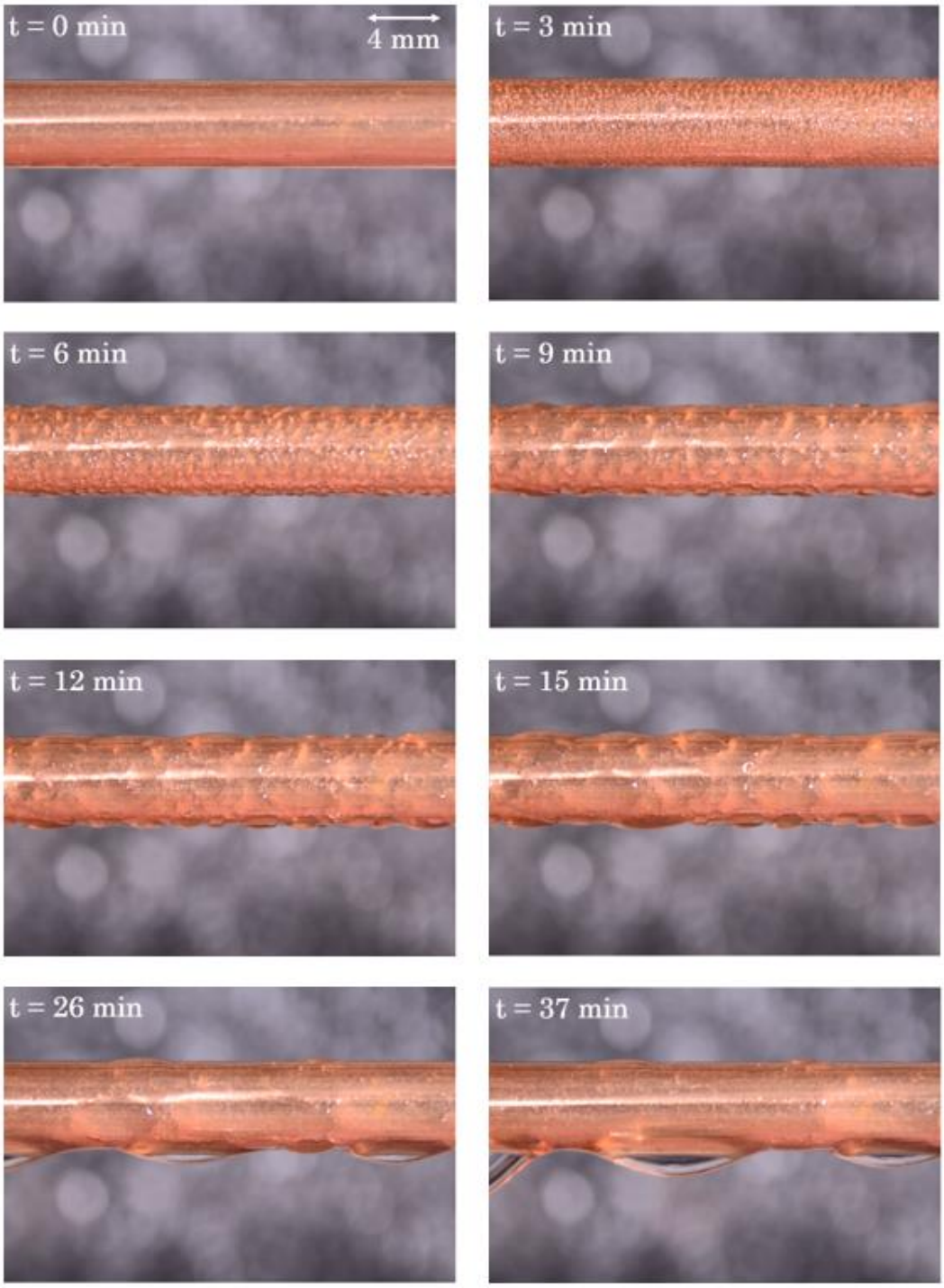

Figure 3.5: Room Temperature Humid Air, Cu, Initial Film-wise Condensation

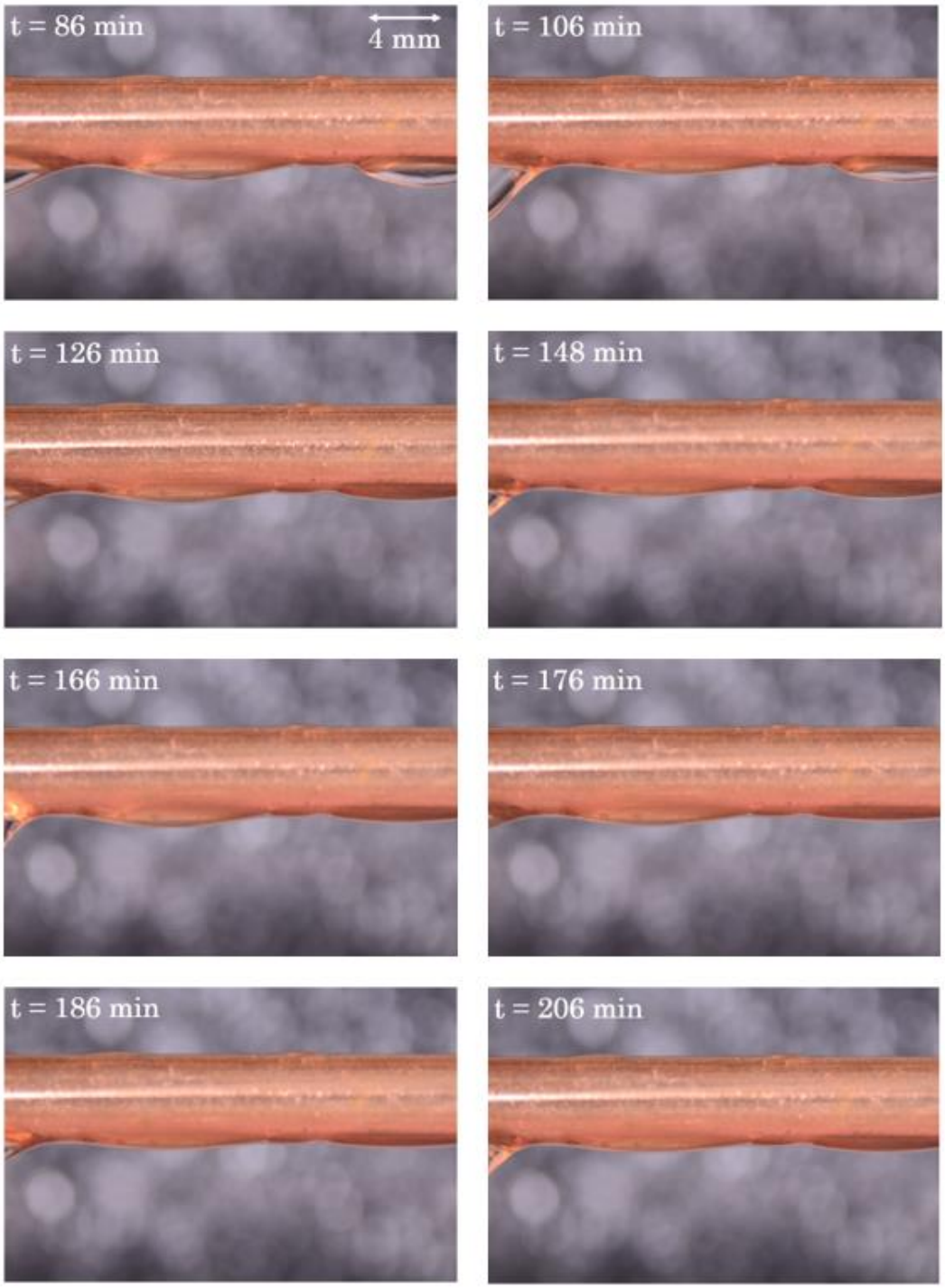

Figure 3.6: Room Temperature Humid Air, Cu, Later Film-wise Condensation

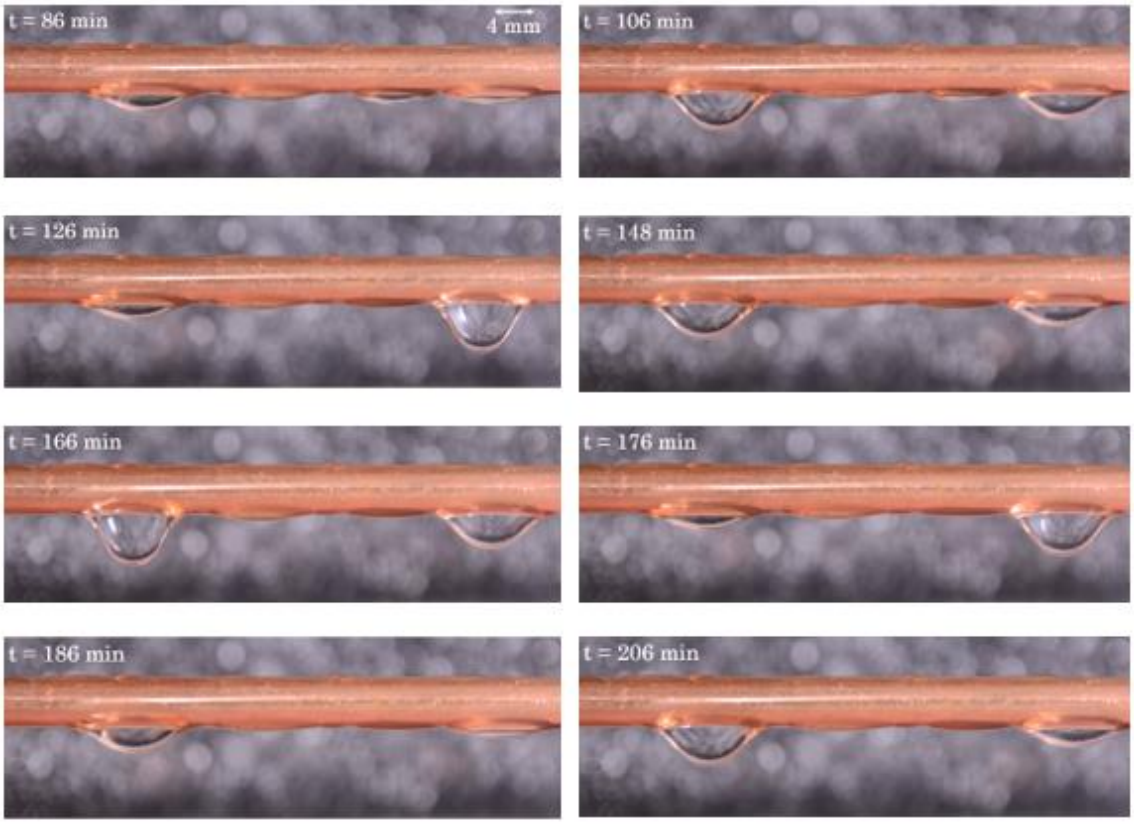

Figure 3.7: Room Temperature Humid Air, Cu, Later Film-wise Condensation (Wide Angle Shot)

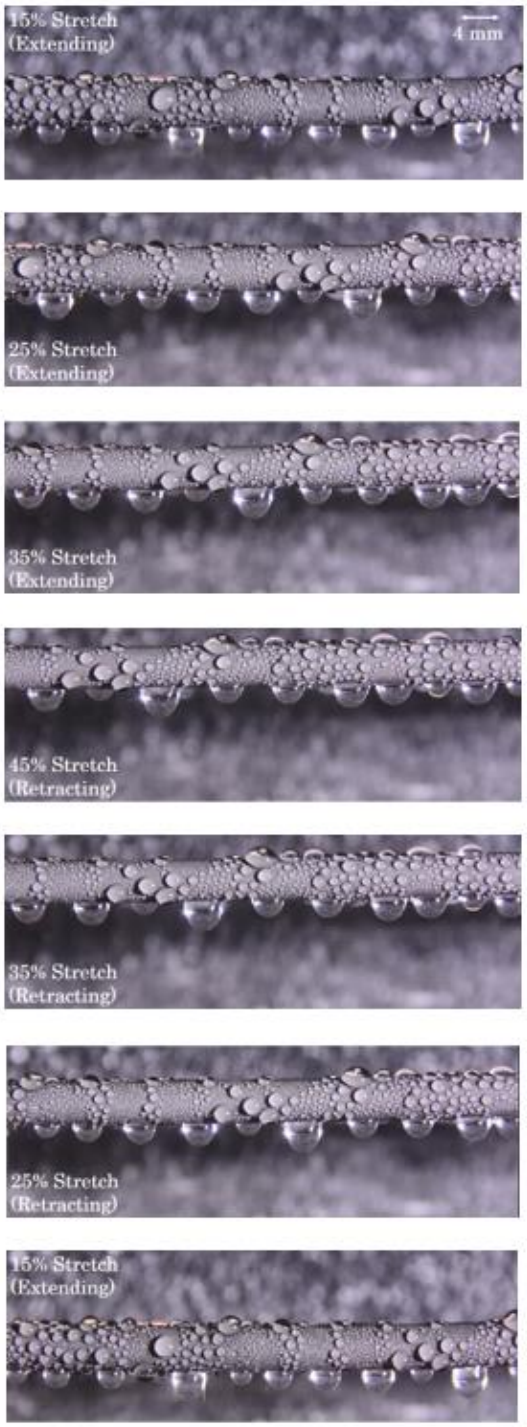

Figure 3.8: Room Temperature Humid Air, LM, 15-45% Stretch (at 9mm/s)

3.2 Hot Humid Air Results

Hot humid air ($\sim 44 - 45°C$ *wet and dry bulb*, $\sim 100\%$ *RH*) with light convective parallel flow tests are conducted according to the parameters specified in Table 2.1. Multiple tests are conducted on a soft thermally enhanced tube at various actuation rates as well as on a static copper reference tube as a benchmark. The raw system thermal resistance R_{sys} is plotted as a function of the tube's nominal actuation rate (mm/s) and displayed as individual data points below.

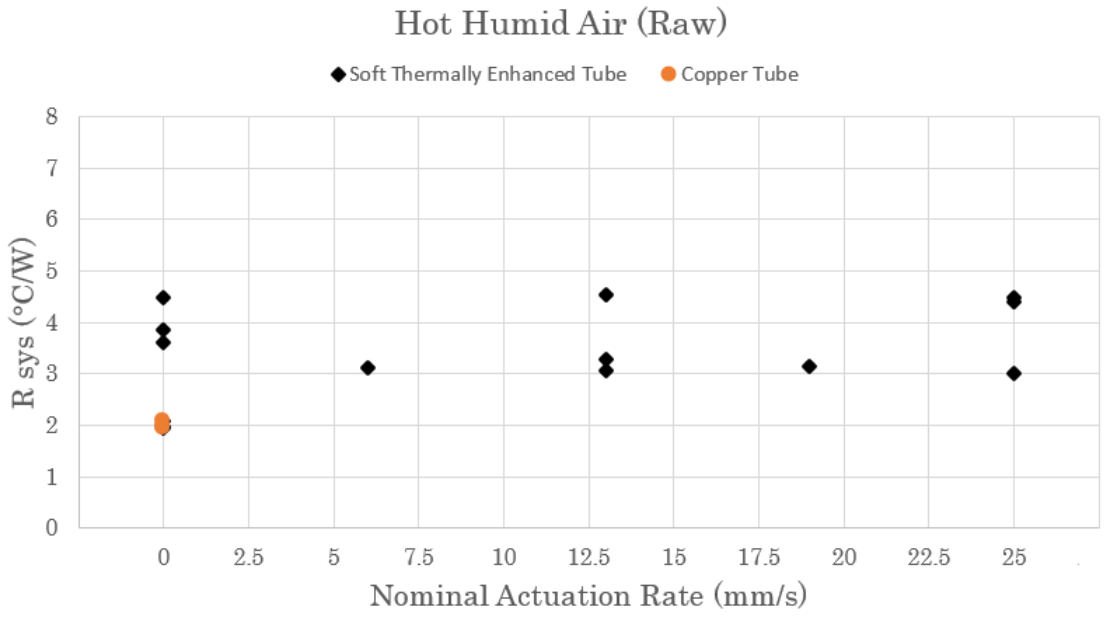

Figure 3.9: Hot Humid Air Raw Data

A non-dependent relation between R_{sys} and the nominal actuation rate is seen from the raw data. It is observed that adjusting the nominal actuation rate does not appreciably change the R_{sys} values for the soft thermally enhanced tube. Therefore, under these hot humid air conditions, adding periodic mechanical stretching and retracting to a soft thermally enhanced tube does not appear to cause

a detectable change in net condensation heat transfer. It is also observed that the copper reference tube, as might be expected a priori, is the lowest R_{sys}. Recall that under room temperature humid air conditions the temperature drop occurring across the water flowing through the DUT is $\sim 0.2°C - 0.4°C$, leading to very high experimental uncertainty due to the low temperature drop. In the case of hot humid air, the temperature drop occurring across the water flowing through the DUT is much higher at $\sim 2.0°C - 4.4°C$, reducing the overall uncertainty and allowing for better statistical conclusions to be made. Accounting for the total uncertainty, the averaged R_{sys} values at each actuation rate, along with corresponding error bars encompassing bias and random uncertainties, are displayed below.

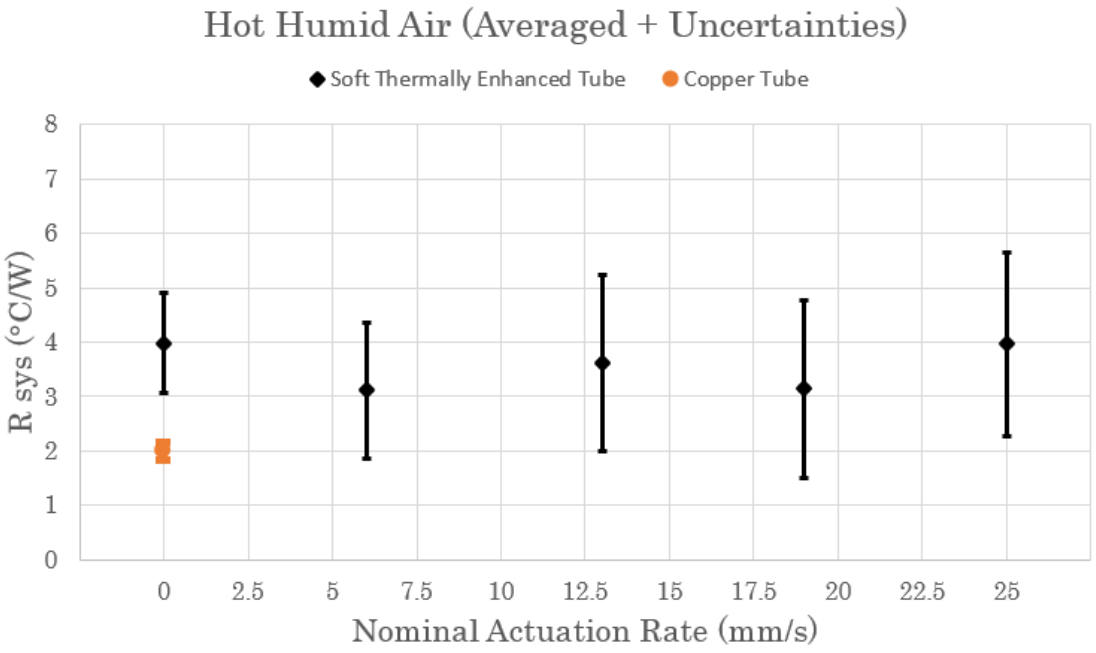

Figure 3.10: Hot Humid Air, Averaged Data with Uncertainties

Note that the error bars shown above for the hot humid air testing are significantly smaller compared to the error bars seen under room temperature

humid air testing. This allows for statistical conclusions to be made with much greater confidence and accuracy. A statistically and physically valid null result is seen, where the nominal actuation rate does not have a statistically significant effect on the system thermal resistance R_{sys}. The copper reference tube has the lowest mean R_{sys} compared to the soft thermally enhanced tube due to its much higher bulk thermal conductivity. The error bars for the soft thermally enhanced tube under most nominal actuation rates are either overlapping or very close to overlapping with the copper reference tube's error bars, suggesting that soft thermally enhanced materials may be a viable alternative to copper for heat transfer condensation applications. Additionally, the contributions of the R_{cond} and $R_{conv,in}$ terms within R_{sys} diminishes the ability to capture differences in $R_{conv,out}$. To better explain this effect, R_{cond} and $R_{conv,in}$ must be estimated.

While R_{cond} is quite difficult to accurately quantify due to uncertainties in the soft thermally enhanced tube's wall thickness and effective thermal conductivity throughout a complete stretch cycle, it can be reasonably approximated by considering only the static condition and assuming static material properties at 30% stretch (corresponding to the midpoint between 15% and 45% stretch). First, the thermal conductivity of the soft thermally enhanced tube held at static 30% condition must be calculated. The thermal conductivity of a composite material, such as a soft thermally enhanced tube, can be estimated using the Maxwell-Garnett model, given as [48]:

$$k_c(\phi) = k_m\left(1 + \frac{3\phi(\delta - 1)}{2 + \delta - \phi(\delta - 1)}\right) \tag{3.1}$$

Where k_c is the composite thermal conductivity ($Wm^{-1}{}^{\circ}C^{-1}$), k_m is the matrix material thermal conductivity ($Wm^{-1}{}^{\circ}C^{-1}$), ϕ is the volume fraction of filler particles to matrix material, and $\delta = k_p/k_m$, where k_p is the filler particle thermal conductivity ($Wm^{-1}{}^{\circ}C^{-1}$).

Assuming that the matrix is pure silicone ($k_m = 0.2\ Wm^{-1}{}^{\circ}C^{-1}$), the filler particles are pure Galinstan ($k_p = 17\ Wm^{-1}{}^{\circ}C^{-1}$), and that the volume fraction is 20% ($\phi = 0.2$), the resulting soft thermally enhanced tube wall conductivity is $k_c = k_{wall} = 0.34\ Wm^{-1}{}^{\circ}C^{-1}$. However, this calculation does not account for the stretching of the tube causing the conductivity to increase, an effect known from past research on similar composites [9, 10].

Additional research on similar soft thermally enhanced tubes [45] shows an increase in thermal diffusivity α from $\alpha = 0.34\ mm^2/s$ at 0% stretch to an estimated $\alpha = 0.46\ mm^2/s$ at 45% stretch, an increase in α of 35%. This increase in thermal diffusivity is estimated to be purely due to changes in thermal conductivity, and not specific heat capacity or density; therefore, it is expected that k_{wall} should also increase by 35% of its 0% stretch value when it is stretched to 45% extension. For a device stretched only from 0% stretch to 30% stretch, this expected percentage increase in thermal conductivity (assuming a linear relation) is 23%. Therefore, it is estimated that $k_{wall} = 0.42\ Wm^{-1}{}^{\circ}C^{-1}$ at 30% stretch.

The wall thickness can be estimated using Equation 2.1 with $L_0 = 271mm$, $\nu = 0.49$, and with unstretched inner-diameter and outer-diameter of $1.96mm$ and $5.24mm$ respectively. At 30% stretch the result is an estimated inner radius of $r_{in} = 0.86\ mm$ and outer radius $r_{out} = 2.30\ mm$. These values yield an estimated wall resistance value of $R_{cond} = 1.06\ ^{\circ}C/W$.

The $R_{conv,in}$ term can be estimated using internal flow convective heat transfer relations. First, it must be determined if the internal flow of liquid water should be regarded as laminar, transitional, and turbulent. The Reynolds number (Re), the dimensionless ratio of inertial to viscous effects of a moving fluid [5], is used. The Reynolds number can be defined as:

$$Re \equiv \frac{UL_{char}}{\nu} \tag{3.2}$$

Where U is the fluid's mean velocity (ms^{-1}), L_{char} is the characteristic length (m), and ν is the fluid's kinematic viscosity (m^2s^{-1}). For the given geometry, flow conditions, and assuming a liquid water kinematic viscosity of $\nu = 0.875 * 10^{-6}\ m^2s^{-1}$ [5], the resulting Reynolds number is $Re \sim 200$. Since a common criterion for laminar heat transfer relations in internal pipe flow is $Re < 2100$ [5], the internal water flow within the tube can be considered (for heat transfer relation purposes) to be decidedly laminar. Therefore, a laminar internal flow convective heat transfer relation for pipes can be used. For this, first consider the Nusselt number definition:

$$Nu \equiv \frac{hL_{char}}{k} \tag{3.3}$$

Where Nu is the Nusselt number (dimensionless ratio of convective to conductive heat flow across a boundary layer), h is the heat transfer coefficient ($Wm^{-2\circ}C^{-1}$), L_{char} is the geometry's characteristic length (m), and k is the fluid's thermal conductivity ($Wm^{-1\circ}C^{-1}$). For laminar internal flow within a pipe with constant heat flux, it can be assumed that $Nu = 4.36$ [5] and that the characteristic

length is the pipe's inner diameter. The resulting internal heat transfer coefficient for the given geometry and flow conditions is therefore $h = h_{in} = 1520\ Wm^{-2}{}^{\circ}C^{-1}$, yielding an estimated internal convective resistance of $R_{conv,in} = 0.35\ ^{\circ}C/W$.

Finally, consider the average data from the static thermally enhanced tube at 30% stretch, where it is found that $R_{sys} = 3.98\ ^{\circ}C/W$. From this system thermal resistance and with estimated values of $R_{conv,in} = 0.35\ ^{\circ}C/W$ and $R_{cond} = 1.06^{\circ}C/W$, the resulting estimated outer convective resistance is therefore $R_{conv,out} = 2.57\ ^{\circ}C/W$. Note that while the outer convective resistance (due primarily to condensation) is the dominant term, it is still approximately the same order of magnitude as the combined effects of the internal convective resistance and wall resistance ($O[R_{conv,out}] \sim O[R_{conv,in} + R_{cond}]$). This acts to obfuscate any changes in R_{sys} that are due to changes in $R_{conv,out}$ alone. An ideal experimental setup to detect such changes would instead have $O[R_{conv,out}] > O[R_{conv,in} + R_{cond}]$, and might be realistically realized by utilizing a soft thermally enhanced tube with a larger internal diameter, a thinner wall thickness, and/or a higher bulk conductivity, all of which would act to decrease the magnitude of the $R_{conv,in}$ and R_{cond} terms.

CHAPTER 4

CONCLUSIONS

4.1 Key Takeaways

The performance of conventional dehumidifiers is limited by the rate at which they can remove condensed water droplets, and typical dehumidification devices rely only on gravity alone to shed droplets once they reach a critical mass. Additionally, conventional dehumidifiers typically use hard metallic tubing due to its ubiquity, durability, and high thermal conductivity, but most hard metals are inherently non-ideal for purely condensation heat transfer due to their hydrophilic nature and their promotion of ineffective film-wise condensation. Soft materials, on the other hand, are generally hydrophobic and therefore promote the substantially more effective drop-wise condensation mode. Soft materials also promote higher nucleation density as well. The primary thermal drawbacks of soft materials in condensation applications are their overall low bulk thermal conductivity and their droplet pinning effect. This work aims to address these two drawbacks through the addition of thermally conductive liquid metal particles to the soft material to improve the bulk thermal conductivity, as well as through the introduction of periodic axial stretching and retracting to the condenser tube to potentially promote more frequent droplet coalescence and shedding.

In these experiments, a soft thermally enhanced tube is created by combining conductive Galinstan liquid metal filler particles with a soft silicone matrix and casting into a tube shape to create a soft thermally enhanced tube. The soft thermally enhanced tube is internally cooled by liquid water and placed in a humid

environment, causing condensation to occur on the exterior surface of the tube and adding heat to the internally flowing water due to both sensible and latent heating effects. The tube is subjected to periodic axial stretching and retracting at various rates via an electric linear actuator, and the effect of this dynamic mechanical movement on droplet shedding (and therefore overall condensation heat transfer) is experimentally investigated using a system thermal resistance heat transfer criterion.

With room temperature humid air conditions ($\sim 20°C\ dry\ bulb, 65-70\%\ RH$), the overall low amount of heat transfer occurring adds significant testing bias variability that makes it difficult to observe any clear trends, and no valid conclusions can be reached from the room temperature humid air data. Real-time imaging is used to show the time dependent formation, growth, and departure images of the condensed droplets.

With hot humid air conditions ($\sim 44-45°C, 100\%\ RH$), a statistically and physically valid null result is detected. Periodic axial stretching and retracting does not cause a statistically significant change in the system thermal resistance, and therefore is not predicted to cause any thermally and statistically significant changes in droplet shedding.

While these results are valid for the particular devices tested in this study, they should not be regarded as an automatic and universal repudiation of the overall concept of using mechanical stretching of soft devices to improve condensed droplet shedding. It should be noted that these results are valid for devices of the types, dimensions, and test conditions detailed in Chapter 2. Alternate devices tested

under different conditions could shed more light on the feasibility of mechanical movement to improve condensed droplet shedding.

4.2 Improvements and Potential Future Studies

A number of potential improvements could be made for any related future studies. The following section aims to recommend some potential improvements in the test setup and hardware itself, as well as potential alternate modes of droplet shedding that could be investigated to improve condensation heat transfer on similar tube devices.

The test hardware could be improved by using a proper engineering environmental chamber (with precisely and independently controllable temperature and RH) in lieu of the custom-made acrylic wind tunnel and PVC bubbler. The current acrylic wind tunnel design is difficult to fully seal, and some test-to-test variability is observed that appears to be correlated with varying methods of patching and sealing the tunnel, which adds to the overall error bars. Additionally, when running the hot humid air case with the current acrylic wind tunnel design, unintended condensation occurs on all internal walls of the acrylic wind tunnel (due to them being unheated and therefore below the local dewpoint temperature) and shed droplets from the top internal wall may interfere with the shedding of droplets on the DUT. An environmental chamber would remove much of this variability and would also remove much of the forced convection crossflow heating effect seen when pumping humid air through a tunnel. It would also provide more working room for a heater surface to be installed to the top wall, allowing the top surface of the chamber to be heated above dew point temperature and removing the effect of condensed

water droplets within the chamber falling on to the DUT and affecting the shedding. The current bubbler design works remarkably well for delivering high RH or saturated humid air but is not independently controllable to a particular RH output. An environmental chamber would allow the RH to be dialed in to a precise value, allowing for varying amounts of condensation and dew point temperatures to be tested.

The test hardware could additionally be improved by using a much larger stretchable thermally enhanced tube with a larger external surface area and/or a large number of stretchable thermally enhanced tubes in parallel. This would increase the surface area for condensation to occur on, allowing for any condensation dependent effects to be detected with better accuracy. Such an approach would have to be balanced with the cost (both time and monetary) in casting a large volume of thermally enhanced soft tubes. Initial proof-of-concept tests could test pure silicone tubes to save on cost, then move on to thermally enhanced devices if potentially promising results are discovered. Improved methods for casting a larger number of thermally enhanced tubes in bulk would greatly expedite the process.

As mentioned in Chapter 3.2, another possible improvement is utilizing a soft thermally enhanced tube with a larger internal diameter, a thinner wall thickness, and a higher bulk conductivity. These alterations would increase the contribution of the outer convective resistance to the overall system thermal resistance and would allow for changes in the outer convective resistance (due to increased droplet shedding and therefore improved condensation) to be more easily detected.

Additional modes of actuation could be investigated with the existing hardware. This study considers only constant periodic actuation, but the setup could

be relatively easily modified to instead hold the DUT static at an extended length, allowing droplets to grow on a large surface area, then quickly retracting to encourage droplet coalescence before returning to a static extended length. If an encouraging correlation is found, it could be insightful to investigate if an optimal condition can be found between both maximizing the condensation HTC and minimizing the amount of work needed to actuate the device.

Additional methods of encouraging droplet departure aside from axial movements could be investigated. Torsional strain could force adjacent droplets to coalesce and would move droplets on the top of the tube to the bottom (and vice versa), which could yield surprising results. "Plucking" of the tube (much like a guitar string) could be used to encourage droplet departure through sudden acceleration and deceleration. Various mechanical vibrational frequencies could be investigated, and the matching of the frequency to the tube's natural frequency could yield some interesting results. Sudden acceleration in the axial direction could encourage enhanced droplet shedding. Compressed gas could be used to periodically shed condensed droplets from the surface and could even be investigated as a method of improving droplet departure on hydrophilic metal condenser surfaces. If an encouraging correlation is found, further testing could be done to look for an optimal condition between both maximizing the condensation HTC and minimizing the total mechanical work needed to compress the gas and/or or the total volume of compressed gas dispensed.

REFERENCES

[1] X. Zhang, B. Sahlberg, G. Wieslander, C. Janson, G. Thorarinn and D. Norback, "Dampness and moulds in workplace buildings: Associations with incidence and remission of sick building syndrome (SBS) and biomarkers of inflammation in a 10 year follow-up study," *Science of the Total Environment,* no. 430, pp. 75-81, 2012.

[2] W.-X. Chu, C.-H. Chiu and C.-C. Wang, "Improvement on dehumidifier performance using a plastic assisted condenser," *Applied Thermal Engineering,* no. 167, 2020.

[3] Y. A. Cengel and M. A. Boles, Thermodynamics An Engineering Approach, New York: McGraw-Hill, 2011.

[4] "Metals, Metallic Elements and Alloys - Thermal Conductivites," Engineering ToolBox, 2005. [Online]. Available: https://www.engineeringtoolbox.com/thermal-conductivity-metals-d_858.html. [Accessed March 2022].

[5] D. A. Kaminski and M. K. Jense, Introduction to Thermal and Fluids Engineering, John Wiley & Sons, Inc., 2005.

[6] E. H. Wissler, Human Temperature Control: A Quantitative Approach, Berlin: Springer, 2018.

[7] Intertronics Co., "Technical Bulletin Thermally Conductive Silicones," October 2018. [Online]. Available: https://www.intertronics.co.uk/wp-content/uploads/2016/11/TB2007-12-Thermally-Conductive-Silicones.pdf. [Accessed March 2022].

[8] A. Fassler and C. Majidi, "Liquid-Phase Metal Inclusions for a Conductive Polymer Composite," *Advanced Materials,* no. 27, pp. 1928-1932, 2015.

[9] M. D. Bartlett, N. Kazem, M. J. Powell-Palm, X. Xhuang, S. Wenhuan, J. A. Malen and C. Majidi, "High thermal conductivity in soft elastomers with elongated liquid metal inclusions," *Proceedings of the National Academy of Sciences ,* vol. 114, no. 9, pp. 2143-2148, 2017.

[10] R. Tutika, S. H. Zhou, M. D. Napolitano and M. D. Bartlett, "Mechanical and Functional Tradeoffs in Multiphase Liquid Metal, Solid Particle Soft Composites," *Advanced Functional Materials,* vol. 28, no. 45, 2018.

[11] E. J. Markvicka, M. D. Bartlett, X. Huang and C. Majidi, "An autonomously electrically self-healing liquid metal–elastomer composite for robust soft-matter robotics and electronics," *Nature Materials,* vol. 14, pp. 618-624, 2018.

[12] J. Tang, X. Zhao, J. Li, R. Guo, Y. Zhou and J. Liu, "Gallium-Based Liquid Metal Amalgams: Transitional-State Metallic Mixtures (TransMixes) with Enhanced and Tunable Electrical, Thermal, and Mechanical Properties," *ACS Applied Materials & Interfaces,* no. 9, pp. 35977-35987, 2017.

[13] W. Kong, W. Zhongyon, M. Wang, K. C. Manning, A. Uppal, M. D. Green, R. Y. Wang and K. Rykaczewski, "Oxide-Mediated Formation of Chemically Stable Tungsten–Liquid Metal Mixtures for Enhanced Thermal Interfaces," *Advanced Materials,* no. 31, 2019.

[14] M. I. Ralphs, N. Kemme, P. B. Vartak, E. Joseph, S. Tipnis, S. Turnage, K. N. Solanki, R. Y. Wang and K. Rykazcewski, "In Situ Alloying of Thermally Conductive Polymer Composites by Combining Liquid and Solid Metal Microadditives," *ACS Applied Materials & Interfaces,* no. 10, pp. 2083-2092, 2018.

[15] M. Ralphs, W. Kong, R. Y. Wang and K. Rykaczewski, "Thermal Conductivity Enhancement of Soft Polymer Composites through Magnetically Induced Percolation and Particle–Particle Contact Engineering," *Advanced Materials Interfaces,* no. 6, 2019.

[16] A. Uppal, M. Ralphs, W. Kong, M. Hart, K. Rykaczewski and R. Y. Wang, "Pressure-Activated Thermal Transport via Oxide Shell Rupture in Liquid Metal Capsule Beds," *ACS Applied Materials & Interfaces,* no. 12, pp. 2625-2633, 2020.

[17] S. A. Nunneley, "Water cooled garments: A review," *Space life sciences,* no. 2, pp. 335-360, 1970.

[18] D. P. Cadogan, "The Past and Future Space Suit," *American Scientist,* vol. 103, no. 5, pp. 338-347, 2015.

[19] NASA, "Liquid Cooled Garments," Midwest Research Institute , Kansas City, 1975.

[20] J.-H. Kim, A. Coca, J. W. Williams and R. J. Roberge, "Effects of Liquid Cooling Garments on Recovery and Performance Time in Individuals Performing Strenuous Work Wearing a Firefighter Ensemble," *Journal of Occupational and Environmental Hygiene,* no. 8, pp. 409-416, 2011.

[21] A. Floruis and S. Cheung, "Design and Control Optimization of Microclimate Liquid Cooling Systems Underneath Protective Clothing," *Annals of Biomedical Engineering,* vol. 34, no. 3, pp. 359-372, 2006.

[22] NASA, "BIO-THERMAL RESPONSES TO VARIED WORK PROGRAMS IN MEN KEPT THERMALLY NEUTRAL BY WATER COOLED CLOTHING," Webb Associates, Inc, Yellow Springs, 1967.

[23] D. Kim, J. Ahn, O. Campbell, N. Paine and L. Sentis, "Investigations of a Robotic Test Bed With Viscoelastic Liquid Cooled Actuators," *IEEE/ASME Transactions on Mechatronics,* vol. 23, no. 6, pp. 2704-2714, 2018.

[24] J. Kendrick, *Design of High-Performance, Dual-Motor Liquid-Cooled, Linear Series Elastic Actuators for a Self-Balancing Exoskeleton (Master's Thesis),* Blacksburg: Virginia Tech, 2018.

[25] D. Kim, O. Campbell, J. Ahn, L. Sentis and N. Paine, "Investigations of Viscoelastic Liquid Cooled Actuators Applied for Dynamic Motion Control of Legged Systems," Birmingham, IEEE-RAS 17th International Conference on Humanoid Robotics (Humanoids).

[26] S. S. Cheng, Y. Kim and J. P. Desai, "Modeling and characterization of shape memory alloy springs with water cooling strategy in a neurosurgical robot," *Journal of Intelligent Material Systems and Structures,* vol. 28, no. 16, pp. 2167-2183, 2017.

[27] Q. Liu, B. Tian, C. Luo, L. Jiang and W. Wu, "Printed Flexible Heaters-Based Thermotherapy Platform for Multiduty Thermal Management," *Advanced Materials Technologies,* no. 5, 2020.

[28] P. Kotagama, A. Phadnis, K. C. Manning and K. Rykaczewski, "Rational Design of Soft, Thermally Conductive Composite Liquid-Cooled Tubes for Enhanced Personal, Robotics, and Wearable Electronics Cooling," *Advanced Materials Technologies,* no. 4, 2019.

[29] K. Rykaczewski, "Rational design of sun and wind shaded evaporative cooling vests for enhanced personal cooling in hot and dry climates," *Applied Thermal Engineering,* no. 171, 2020.

[30] J. H. Cho, D. J. Preston, Y. Zhu and E. N. Wang, "Nanoengineered materials for liquid–vapour phase-change heat transfer," *Nature Reviews Materials,* vol. 2, no. 16092, 2016.

[31] E. Schmidt, W. Schurig and W. Sellschopp, "Versuche uber die Kondensation in Film- und Tropfenform," *Tech. Mech. Thermodynamik,* vol. I, pp. 53-63, 1930.

[32] CORROSIONPEDIA, "Young's Equation," Corrosionpedia Inc., 2022. [Online]. Available: https://www.corrosionpedia.com/definition/7138/youngs-equation-liquids. [Accessed April 2022].

[33] R. W. Style, A. Jagota, C.-Y. Hui and E. R. Dufresne, "Elastocapillarity: Surface Tension and the Mechanics of Soft Solids," *Annual Review of Condensed Matter Physics,* vol. 8, pp. 99-118, 2017.

[34] A. Rusanov, "On the thermodynamics of deformable solid surfaces," *Journal of colloid and interface science,* vol. 63, no. 2, pp. 330-345, 1978.

[35] Y.-S. Yu and Y.-P. Zhao, "Elastic deformation of soft membrane with finite thickness induced by a sessile liquid droplet," *Journal of Colloid and Interface Science,* no. 339, pp. 489-494, 2009.

[36] R. Pericet-Camara, A. Best, H.-J. Butt and E. Bonaccurso, "Effect of Capillary Pressure and Surface Tension on the Deformation of Elastic Surfaces by Sessile Liquid Microdrops: An Experimental Investigation," *American Chemical Society,* vol. 24, pp. 10565-10568, 2008.

[37] R. Pericet-Camara, G. K. Auernhammer, K. Koynov, S. Lorenzoni, R. Raiteri and E. Bonaccurso, "Solid-supported thin elastomer films deformed by microdrops," *Soft Matter,* vol. 5, no. 19, pp. 3611-3617, 2009.

[38] A. Phadnis and K. Rykaczewski, "Dropwise Condensation on Soft Hydrophobic Coatings," *Langmuir,* vol. 33, no. 43, pp. 12095-12101, 2017.

[39] M. Sokuler, G. K. Auernhammer, M. Roth, C. Liu, E. Bonacurrso and H.-J. Butt, "The Softer the Better: Fast Condensation on Soft Surfaces," *Langmuir,* vol. 26, no. 3, pp. 1544-1547, 2010.

[40] I. Oh, H. Cha, J. Chen, S. Chavan, H. Kong, N. Miljkovic and Y. Hu, "Enhanced Condensation on Liquid-Infused Nanoporous Surfaces by Vibration-Assisted Droplet Sweeping," *ACS Nano,* vol. 14, no. 10, pp. 13367-13379, 2020.

[41] ThoughtCo., "Profile of the Metal Galinstan," Dotdash Meredith, 03 Frbuary 2020. [Online]. Available: https://www.thoughtco.com/what-is-galinstan-2340177. [Accessed April 2022].

[42] Chemistry Learner, "Galinstan," 2022. [Online]. Available: https://www.chemistrylearner.com/galinstan.html. [Accessed April 2022].

[43] P. Xiao, J.-H. Kim and S. Seo, "Flexible and Stretchable Liquid Metal Electrodes Working at Sub-Zero Temperature and Their Applications," *Materials,* vol. 14, 2021.

[44] K. Larson, "Dow White Paper, Can You Estimate Modulus From Durometer Hardness for Silicones?," 2019. [Online]. Available: https://www.dow.com/content/dam/dcc/documents/en-us/tech-art/11/11-37/11-3716-01-durometer-hardness-for-silicones.pdf. [Accessed April 2022].

[45] P. Kotagama, "Fundamentals of Soft, Stretchable Heat Exchanger Design (Doctoral Dissertation)," ASU , Tempe, 2020.

[46] O. O. Parish and T. W. Putnam, "NASA TECHNICAL NOTE EQUATIONS FOR THE DETERMINATION OF HUMIDITY FROM DEWPOINT AND PSYCHROMETRIC DATA," Dryden Flight Research Center, Washington, D.C., 1977.

[47] J. Mandel, The Statistical Analysis of Experimental Data, New York: Dover Publications, Inc., 1964.

[48] C. Hongyu, V. V. Ginzburg, J. Yang, Y. Yang, W. Liu, Y. Huang, L. Du and B. Chen, "Thermal conductivity of polymer-based composites: Fundamentals and applications," *Progress in Polymer Science,* no. 59, pp. 41-85, 2016.

APPENDIX A

TEST PARAMETER DETAILS

Laptop #	Data Source	Test Parameter	Symbol	Units	Used in Post Processing?	Comments
1	PTC10 Thermocouple Reader	Water inlet temperature	$T_{w,in}$	$°C$	Yes	36 gauge T-Type SLE Thermocouple
1	PTC10 Thermocouple Reader	Water outlet temperature	$T_{w,out}$	$°C$	Yes	36 gauge T-Type SLE Thermocouple
1	PTC10 Thermocouple Reader	Tunnel inlet temperature	N/A	$°C$	No	Thin Probe T-Type Thermocouple
1	PTC10 Thermocouple Reader	Laboratory ambient temperature	N/A	$°C$	No	Thin Probe T-Type Thermocouple
1	Arduino Uno #1	Actuator state	N/A	N/A	No	"Extension" or "Retraction"
1	Arduino Uno #1	DUT current length	N/A	mm	No	-
1	Arduino Uno #1	Water flowrate	N/A	$None$	No	0-1023 analog output only
2	Arduino Uno #2	Air temp. at beginning of DUT	$T_{a,in}$	$°C$	Yes	Measured by TH1 sensor
2	Arduino Uno #2	RH at beginning of DUT	RH_{in}	$None$	Yes	Measured by TH1 sensor
2	Arduino Uno #2	Air temp. at middle of DUT	$None$	$°C$	No	Measured by TH2 sensor
2	Arduino Uno #2	RH at middle of DUT	$None$	$None$	No	Measured by TH2 sensor

2	Arduino Uno #2	Air temp. at end of DUT	$None$	$°C$	No	Measured by TH3 sensor
2	Arduino Uno #2	RH at end of DUT	$None$	$None$	No	Measured by TH3 sensor
2	Arduino Uno #2	Laboratory ambient temperature	$None$	$°C$	No	Measured by TH4 sensor (ambient)
2	Arduino Uno #2	Laboratory ambient RH	$None$	$None$	No	Measured by TH4 sensor (ambient)
N/A	Manual totalizing in beaker	Water flowrate	$\dot{m}$	ml/min	Yes	Assuming 1 ml/s = 0.001 kg/s
N/A	Analog press. Gauge	Water pressure	$None$	psi	No	-
N/A	Digital gas volumetric flowmeter	Dry air volumetric flowrate	$None$	L/min	No	Used to manually dial in flowrate
N/A	Analog press. Gauge	Dry air pressure	$None$	psi	No	-
N/A	Temperature controller	Bubbler temperature	$None$	$°C$	No	Used to verify bubbler temp.
N/A	Chiller	Chiller temperature	$None$	$°C$	No	Used to verify chiller temp.

APPENDIX B

SUMMARY DATA DETAILS

Date	Tube	Rate (mm/s)	Trial #	A. File Good?	mdot H2O (ml/min)	Vdot Dry Air (L/min)	Air P (psi)
11/4/2021	LM	5	1	Y	50	50	4.5
11/5/2021	LM	1	1	Y	52	49	4.5
11/6/2021	LM	9	1	Y	51	50	4.75
11/7/2021	LM	0	1	Y	51	46.5	4.5
12/2/2021	LM	0	2	Y	52	47	4.5
12/7/2021	LM	1	2	Y	53	51.5	4.5
12/9/2021	LM	5	2	Y	51.5	53	4.5
12/14/2021	LM	9	2	Y	52	54	4.75
12/22/2021	LM	25	1	Y	49.5	51.5	4.5
12/23/2021	LM	25	2	Y	51	50	4.75
11/14/2021	Cu	0	1	Y	52	52	4.75
11/30/2021	Cu	0	2	Y	53	51.5	4.5

L10M, dT H2O	L10M, Qwater	L10M, DP T (TH1)	L10M, H2O TC In	L10M Rtot (C/W)	Sigma Bias Rtot (C/W)
0.37	1.28	14.03	6.53	5.84	2.21
0.26	0.93	13.85	6.62	7.74	4.14
0.25	0.88	13.93	6.67	8.25	4.59
0.21	0.73	14.09	6.74	10.04	6.58
0.17	0.61	13.89	6.9	11.54	9.37
0.22	0.82	13.8	6.88	8.5	5.43
0.17	0.6	13.54	6.94	11.02	8.93
0.11	0.42	13.77	6.96	16.4	21.85
0.22	0.76	13.23	6.69	8.6	5.49
0.18	0.62	13.91	6.91	11.21	8.53
0.31	1.13	13.89	6.79	6.3	2.86
0.37	1.35	13.9	6.82	5.24	1.97

Room temperature humid air, summary data (12 continuous rows)

Date	Tube	Rate (mm/s)	Trial #	A. File Good?	mdot H2O (ml/min)	Vdot Dry Air (L/min)	Air P (psi)
12/28/2021	LM	0	1	Y	51	52.5	5
12/30/2021	LM	25	1	Y	51	50	4.5
1/1/2022	LM	13	1	Y	51	53	5
1/9/2022	LM	25	2	Y	50	53	5
1/17/2022	LM	0	2	Y	51	53.5	5
2/6/2022	LM	0	3	Y	49	51.5	4.75
2/12/2022	LM	13	2	Y	51	50	4.75
2/20/2022	LM	25	3	Y	51	51.5	4.75
2/21/2022	LM	13	3		51.5	51.5	4.75
3/6/2022	LM	6	1	Y	51	49	4.75
3/14/2022	LM	19	1	Y	52	50	4.5
3/16/2022	Cu	0	1	Y	52	49	4.5
3/20/2022	Cu	0	2	Y	51	48	4.75
3/23/2022	Cu	0	3	Y	50	51.5	4.75

L10M, dT H2O	L10M, Qwater	L10M, DP T (TH1)	L10M, H2O TC In	L10M Rtot (C/W)	Sigma Bias Rtot (C/W)
2	7.1	44.64	12.92	4.47	0.33
2.01	7.12	44.43	13.03	4.41	0.32
1.96	6.96	44.41	12.9	4.53	0.34
2.03	7.04	44.43	12.79	4.49	0.32
2.33	8.26	44.44	12.52	3.86	0.25
2.5	8.53	44.09	13.24	3.62	0.22
2.84	10.06	43.72	13.05	3.05	0.16
2.92	10.36	43.97	12.77	3.01	0.16
2.63	9.42	43.81	13.05	3.27	0.19
2.76	9.78	43.64	13.18	3.12	0.17
2.7	9.74	43.65	13.03	3.14	0.18
4.39	15.85	43.66	12.85	1.94	0.08
4.42	15.66	43.65	12.81	1.97	0.08
4.28	14.86	43.82	13.05	2.07	0.08

Hot humid air data, summary data (14 continuous rows)

APPENDIX C

LINEAR ACTUATOR CALIBRATIONS

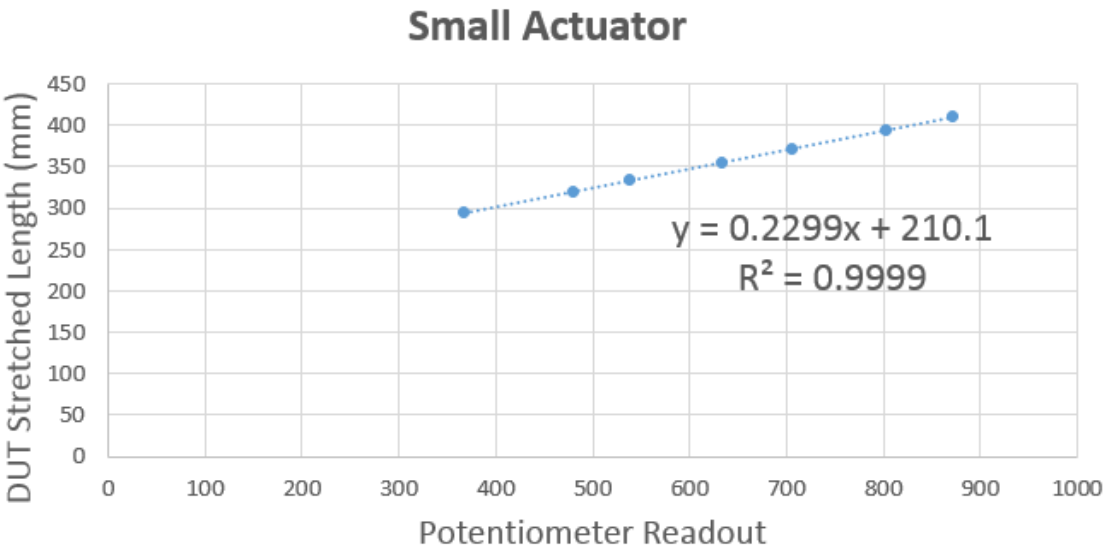
Small Actuator
DUT Stretched Length (mm)
450
400
350
300
250
200
150
100
50
0
0
100
200
300
400
500
600
700
800
900
1000
Potentiometer Readout
y = 0.2299x + 210.1
R² = 0.9999

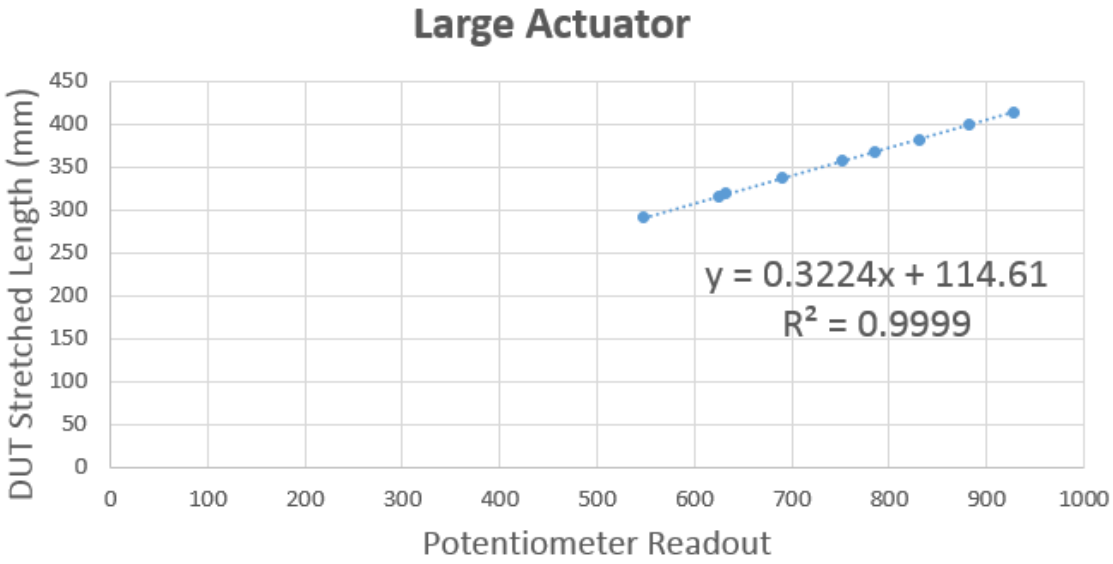
Large Actuator
DUT Stretched Length (mm)
450
400
350
300
250
200
150
100
50
0
0
100
200
300
400
500
600
700
800
900
1000
Potentiometer Readout
y = 0.3224x + 114.61
R² = 0.9999